

The ALHAMBRA Survey: Bayesian Photometric Redshifts with 23 bands for 3 squared degrees.

A. Molino¹, N. Benítez¹, M. Moles², A. Fernández-Soto³, D. Cristóbal-Hornillos², B. Ascaso¹, Y. Jiménez-Teja¹, W. Schoenell¹, P. Arnalte-Mur⁴, M. Pović¹, D. Coe⁵, C. López-Sanjuan², L. A. Díaz-García², J. Varela², I. Matute¹, J. Masegosa¹, I. Márquez¹, J. Perea¹, A. Del Olmo¹, C. Husillos¹, E. Alfaro¹, T. Aparicio-Villegas^{1,6}, M. Cerviño^{1,7}, M. Huertas-Company^{8,9}, J. A. L. Aguerri⁷, T. Broadhurst¹⁰, J. Cabrera-Caño¹¹, J. Cepa^{7,12}, R. M. González Delgado¹, L. Infante¹³, V. J. Martínez³, F. Prada¹, J. M. Quintana¹

¹IAA-CSIC, Glorieta de la astronomía S/N. 18008, Granada, Spain

²Centro de Estudios de Física del Cosmos de Aragón (CEFCA), Plaza San Juan 1, 44001 Teruel, Spain

³Obs. Ast. Univ. Valencia, Edificio de Institutos, Polígono de la Coma s/n, Paterna-46980-Valencia, Spain

⁴Institute for Computational Cosmology, Department of Physics, Durham University, South Road, Durham DH1 3LE, UK

⁵Space Telescope Science Institute, Baltimore, MD, USA

⁶Observatório Nacional-MCT, Rua José Cristino, 77. CEP 20921-400, Rio de Janeiro-RJ, Brazil

⁷Instituto de Astrofísica de Canarias, Vía Láctea s/n, La Laguna, Tenerife 38200, Spain

⁸GEPI, Paris Observatory, 77 av. Denfert Rochereau, 75014 Paris, France

⁹University Denis Diderot, 4 Rue Thomas Mann, 75205 Paris, France

¹⁰Department of Theoretical Physics, University of the Basque Country UPV/EHU, Bilbao, Spain

¹¹Departamento de Física Atómica, Molecular y Nuclear, Facultad de Física, Universidad de Sevilla, Spain

¹²Departamento de Astrofísica, Facultad de Física, Universidad de la Laguna, Spain

¹³Departamento de Astronomía, Pontificia Universidad Católica. Santiago, Chile

9 October 2018

ABSTRACT

The ALHAMBRA (Advance Large Homogeneous Area Medium Band Redshift Astronomical) survey has observed 8 different regions of the sky, including sections of the COSMOS, DEEP2, ELAIS, GOODS-N, SDSS and Groth fields using a new photometric system with 20 contiguous $\sim 300\text{\AA}$ filters covering the optical range, combining them with deep $JHKs$ imaging. The observations, carried out with the Calar Alto 3.5m telescope using the wide field (0.25 deg^2 FOV) optical camera LAICA and the NIR instrument Omega-2000, correspond to $\sim 700\text{hrs}$ of on-target science images. The photometric system was specifically designed to maximize the effective depth of the survey in terms of accurate spectral-type and photometric redshift estimation along with the capability of identification of relatively faint emission lines. Here we present multicolor photometry and photometric redshifts for $\sim 438,000$ galaxies, detected in synthetic $F814W$ images, complete down to a magnitude $I \sim 24.5\text{AB}$, carefully taking into account realistic noise estimates, and correcting by PSF and aperture effects with the *ColorPro* software. The photometric zeropoints have been calibrated using stellar transformation equations and refined internally, using a new technique based on the highly robust photometric redshifts measured for emission line galaxies. We calculate photometric redshifts with the BPZ2.0 code, which includes new empirically calibrated galaxy templates and priors. Our photometric redshifts have a precision of $\delta_z/(1+z_s)=1\%$ for $I < 22.5$ and $\delta_z/(1+z_s)=1.4\%$ for $22.5 < I < 24.5$. Precisions of $\delta_z/(1+z_s) < 0.5\%$ are reached for the brighter spectroscopic sample, showing the potential of medium-band photometric surveys. The global photometric redshift distribution shows a mean redshift $\langle z \rangle = 0.56$ for $I < 22.5\text{ AB}$ and $\langle z \rangle = 0.86$ for $I < 24.5\text{ AB}$. The data presented here covers an effective area of 2.79 deg^2 , split into 14 strips of $58.5' \times 15.5'$ and represents $\sim 32\text{ hrs}$ of on-target. Given its depth, multiband coverage and a much smaller cosmic variance than other similar projects, ALHAMBRA is a unique dataset for galaxy evolution studies. Several of the techniques presented here will have a wide applicability to future large scale photometric redshift surveys like JPAS.

Key words: catalogs - galaxies: photometric redshifts - surveys: multiwavelength

1 INTRODUCTION

Photometric redshifts (Baum 1962, Lanzetta, Fernández-Soto & Yahil 1997, Benítez 2000) have become a powerful tool for cosmology and galaxy evolution studies. Several photometric surveys, using different filter systems, have been carried out in the last years: the UBC-NASA survey (Hickson & Mulrooney 1998), CADIS (Wolf et al. 2001b), COMBO-17 (Wolf et al. 2001a) and most recently, COSMOS-21 (Taniguchi 2004, Ilbert et al. 2009) or SHARDS (Pérez-González et al. 2013). The ALHAMBRA (Advance Large Homogeneous Area Medium Band Redshift Astronomical) survey (Moles et al. 2008) has been optimized to detect and measure precise and reliable photometric redshifts for a large population of galaxies over 8 different fields. As it was shown in Benítez et al. (2009b), although counterintuitive, broadband photometric surveys can be significantly shallower, in terms of photometric redshift depth, than well designed, medium band imaging. ALHAMBRA uses a specially designed filter system (see also Aparicio-Villegas et al. 2010) which covers the whole optical range (3500Å to 9700Å) with 20 contiguous, equal-width, non overlapping, medium-band filters along with the standard JHKs near-infrared bands, aiming at covering a total area of 4 deg² on the sky separated in 8 non-contiguous regions (Fig. 1).

The photometric system has been specifically designed to optimize photometric redshift depth and accuracy (Benítez et al. 2009b), while keeping the capability of detecting and identifying relatively faint emission lines (Bongiovanni et al. 2010, Matute et al. 2012). The observations presented here were carried out with the Calar Alto 3.5m telescope using both the wide field camera LAICA in the optical range and the Omega-2000 camera in the Near Infrared (NIR) from 2005 to 2012. In order to define a constant and homogeneous window for all the ALHAMBRA fields, we generated synthetic F814W detection images (corresponding to HST/ACS F814W). Since these images are photometrically complete down to a magnitude $F814W \leq 24.5$ and have a much better S/N than individual filters, they represent the best images for source detection. Meanwhile they served to perform direct comparisons with other space-based surveys as COSMOS. Hereafter, F814W magnitudes represent the magnitudes derived on the synthetic F814W images.

In this paper we summarize the ALHAMBRA-survey observations and the data reduction in Section 2. We explain the complete treatment of the photometric catalogues used to derive photometric redshifts in Section 3. This includes the performed aperture-matched PSF-corrected photometry, the generation of synthetic F814W detection images and their corresponding star masking treatment, a statistical star/galaxy classification and an empirical estimation of the photometric uncertainties. We discuss several photometric checks in Section 3.8. Along Section 4 we analyze the methodology used to derive the photometric redshifts, the different methods used to compute photometric zeropoint calibrations and the photometric redshift accuracy quantification as a function of F814W magnitude, redshift and *Odds*. Finally we present the description of the ALHAMBRA photometric redshift catalogues in Section 5.

All optical and near-IR magnitudes in this paper are on the AB system. Cosmological parameters of $H_0 = 70 \text{ km s}^{-1} \text{ Mpc}^{-1}$, $\Omega_M = 0.3$, $\Omega_\Lambda = 0.7$ are assumed throughout.

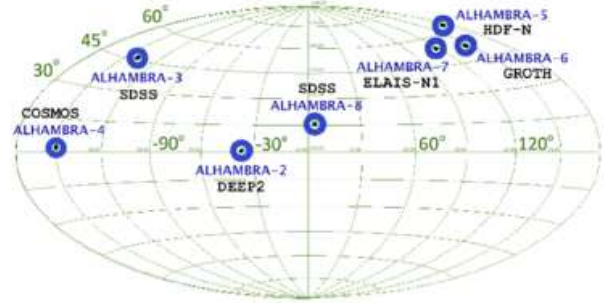


Figure 1. The figure shows the different fields observed by the ALHAMBRA survey along with their correspondence with other existing surveys. The mean galactic coordinates are specified in Table 1.

2 OBSERVATIONS AND DATA REDUCTION

2.1 Observations

The ALHAMBRA-survey has imaged a total area of 4.0 deg² among eight separated regions of the sky during a seven-year period (2005–2012). Observations were carried out on the 3.5m telescope on the Calar Alto Observatory (CAHA, Spain) making use of the two wide-field imagers in the optical (LAICA) and in the NIR (Omega-2000). The ALHAMBRA fields have been observed whenever the conditions were optimal (seeing < 1.6", airmass < 1.8), up to reach a total exposure time of ~700hrs (~32 hrs of on-target). The integration time for individual CCDs was split into ~27.8 hrs for medium-band filters and ~4.2 hrs for broad-band Near Infrared (NIR) filters, as explained in Cristóbal-Hornillos et al. 2013, (in prep.).

Although ALHAMBRA-01 has already been observed, its analysis has not been included in this paper due to issues with its primary photometric calibration at the time. For a detailed description of the NIR observations, we refer the reader to Cristóbal-Hornillos et al. (2009). The description of the optical observations will be available in Cristóbal-Hornillos et al. 2013 (in prep.).

2.2 Data Reduction

In order to homogenize the data sets from both imagers, NIR images from the OMEGA-2000 detector were converted from their original pixel size, 0.45"/pix, to 0.221"/pix to match the pixel size of the LAICA images. This way every detection was referred to the same pixel in either image. As explained in Cristóbal-Hornillos et al. (2009), individual images from each run have been dark current corrected, flat fielded and sky subtracted. Bad pixels, cosmic rays, linear patterns and ghost images have also been masked out. Processed images have been finally combined using SWARP (Bertin et al. 2002) software where applied geometrical distortions have been incorporated in WCS headers.

The total 2.8 deg² included in this work are divided in 7 non-contiguous regions of the sky (as summarized in Table 1), split in non-overlapping strips composed by 4 individual CCDs, as schematically illustrated in Appendix A. Each one of the 48

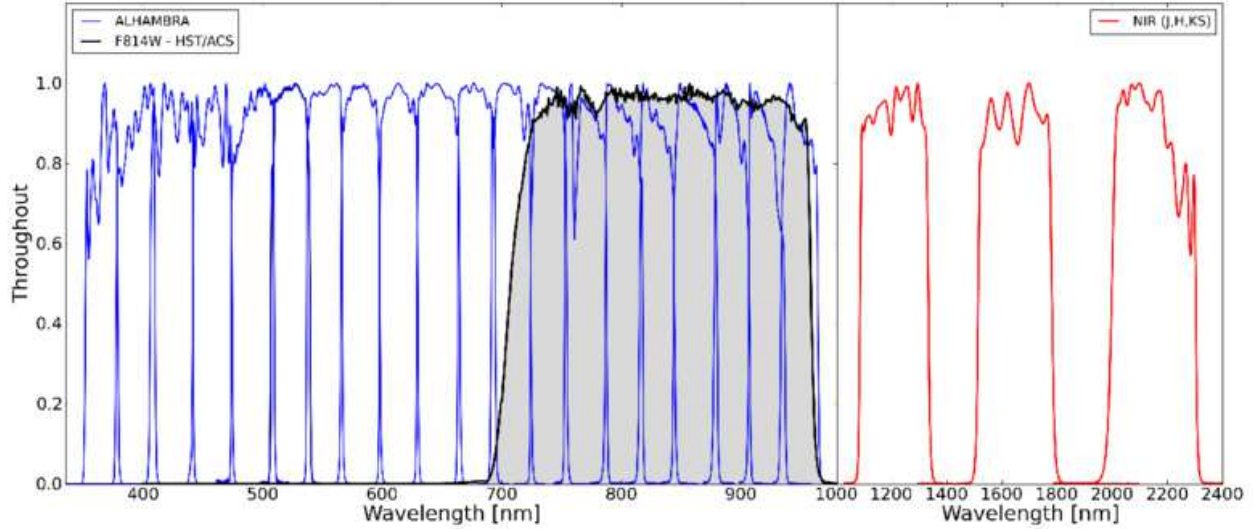


Figure 2. The ALHAMBRA survey filter set. On the left-hand side, solid blue lines represent the Optical filter system composed by 20 contiguous, equal-width, non overlapping, medium-band ($\sim 300\text{\AA}$) filters. The solid black line corresponds to the synthetic F814W filter used to define a constant observational window across fields. On the right-hand side, solid red lines represent the standard *JHKs* near-infrared broad bands. All transmission curves are normalized to its maximum value.

Table 1. The ALHAMBRA survey selected fields

Field Name	Overlapping Survey	RA (J2000)	DEC (J2000)	Area / Effective [deg ²]	Number catalogs	Science Images	Detected ⁽¹⁾ Sources	Density ^(1,2) [# / deg ²]
ALHAMBRA-1	—	00 29 46.0	+05 25 30	0.50 / —	—	192	—	—
ALHAMBRA-2	DEEP2	01 30 16.0	+04 15 40	0.50 / 0.45	8	192	67.791	77.144
ALHAMBRA-3	SDSS	09 16 20.0	+46 02 20	0.50 / 0.47	8	192	68.015	75.000
ALHAMBRA-4	COSMOS	10 00 00.0	+02 05 11	0.25 / 0.23	4	96	38.464	93.261
ALHAMBRA-5	HDF-N	12 35 00.0	+61 57 00	0.25 / 0.24	4	96	42.618	82.300
ALHAMBRA-6	GROTH	14 16 38.0	+52 24 50	0.50 / 0.47	8	192	66.906	77.740
ALHAMBRA-7	ELAIS-N1	16 12 10.0	+54 30 15	0.50 / 0.47	8	192	79.453	82.185
ALHAMBRA-8	SDSS	23 45 50.0	+15 35 05	0.50 / 0.46	8	192	75.109	82.452
				3.00 / 2.79	48	1344	438.356	<81.440>

¹ w/o duplications

² F814W < 24.

CCDs represents the minimum area ($15.5' \times 15.5'$) covered by all the 23 individual filters. To quantify the survey effective area (Section 3.5.3), FLAG images have been created where pixels not satisfying an established photometry quality criteria have been flagged. Meanwhile both RMS-map and WEIGHT-maps have been generated accounting for the level of photometric uncertainties present across individual images.

2.3 Filter set

As it was shown in Benítez et al. (2009b), once the instrumental setup and exposure time are fixed, the filter set has a powerful effect on the photo-z performance. Table 2 summarises a small list of

different photometric filter systems and their photometric redshift accuracy. The ALHAMBRA survey designed its own photometric system (Benítez et al. 2009b) optimizing both photometric depth and accurate measurements for both Spectral Energy Distribution (SED) and photometric redshift identifications for as many galaxies as possible, along with the detectability of relatively faint emission lines. As seen in Fig. 2 the system encompasses an optical window ranging from $3500\text{-}9700\text{\AA}$ discretized in 20 constant-width ($\sim 300\text{\AA}$), non overlapping filters with a NIR window given by the standard Johnson NIR bands *J*, *H* and *Ks*. Including both Optical + NIR observations serves to break the so-called color-redshift degeneracies, reducing the fraction of catastrophic outliers and increasing the ALHAMBRA photometric redshift depth. In Fig. 3

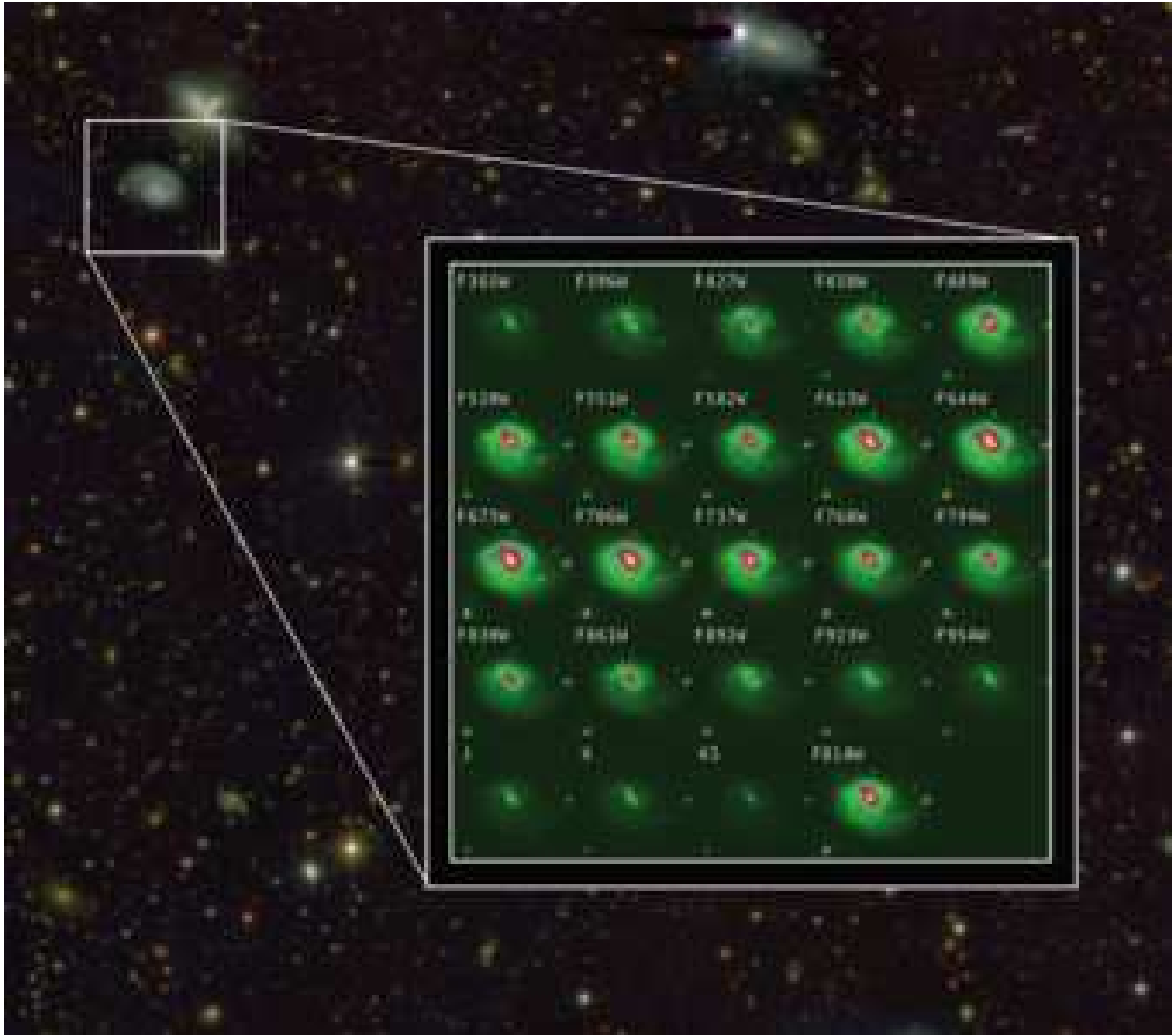


Figure 3. The ALHAMBRA-survey. The figures shows an example about how a galaxy looks like when observed through the ALHAMBRA filter system. While the optical range is spanned horizontally from top to bottom and left to right, the last row corresponds to the J , H and K_s NIR filters along with the synthetic F814W detection image. The background color image was generated using the *Trilog* software (www-int.stsci.edu/~dcoe/trilog/Intro.html).

we show an example about how a galaxy looks like when observed through the ALHAMBRA survey filter system. The main properties for each individual filter are summarized in Table 3.

2.4 Primary photometric zeropoint calibration.

Taking advantage of the overlapping areas between ALHAMBRA and the Sloan Digital Sky Survey (SDSS, York et al. 2000), a set of transformation equations among both (optical) photometric systems was initially derived based on a collection of primary standard stars from the Next Generation Spectral Library (HST/STIS NGSL, Gregg et al. 2004), as explained in Aparicio-Villegas et al. (2010).

An exhaustive identification of good photometric stars in the ALHAMBRA fields has been carried out in such a way that only

the stars with available SDSS/DR7 photometry were kept. Then, transformation equations from the SDSS/DR7 data are used to obtain the Alhambra photometry in each band for the stellar objects. Photometric zeropoints for optical images have been finally determined as the mean difference between instrumental magnitudes (from transformation equations) and synthetic magnitudes (from the transformation equations) yielding an internal error no longer than a few hundredths of magnitude for used stars in each CCD and filter combination. For an in-depth discussion about the calibration of the ALHAMBRA optical photometric system we refer the reader to Cristóbal-Hornillos et al. 2013 (in prep.).

The ALHAMBRA-survey has also made use of the spatial overlapping with the 2MASS catalogue (Cutri et al. 2003) to calibrate its NIR images. As explained in Cristóbal-Hornillos et al. (2009) several tens of common point-like sources with high S/N were selected to compute photometric zeropoint offsets with un-

Table 2. Photometric Redshift Surveys

survey	Reference	Bands	$\delta_z/(1+z)$
HDF	Sawicki (1997)	4	0.080
SDSS/DR6	Csabai (2003)	5	0.035
SWIRE	Rowan-Robinson (2008)	5	0.035
HUDF	Coe (2006)	6	0.040
HDF	Fernández-Soto (1999)	7	0.060
CFHTLS	Ilbert (2006)	9	0.030
GOODS	Dahlen (2010)	12	0.040
CLASH	Molino (2013, prep.)	16	0.025
COMBO-17	Wolf (2004)	17	0.020
ALHAMBRA	Molino (this work)	23	0.013
COSMOS	Ilbert (2009)	30	0.007
MUSYC	Cardamone (2010)	32	0.007
JPAS	Benítez (2009a, 2013, prep.)	59	0.003

Table 3. Summary of the Multiwavelength Filter Set for ALHAMBRA. The FWHM, the exposure time and the limiting magnitude (measured on 3" diameter aperture) correspond to the average value among the 48 CCDs.

CAMERA	FILTER	λ_{eff} [Å]	FWHM [Å]	$\langle t_{exp} \rangle$ [sec]	$\langle m_{lim}^{(3'')} \rangle$ (5- σ)
Optical					
LAICA	F365W	365	279	3918	23.7
LAICA	F396W	396	330	2896	23.8
LAICA	F427W	427	342	2774	23.8
LAICA	F458W	458	332	3079	23.8
LAICA	F489W	489	356	2904	24.2
LAICA	F520W	520	326	2664	24.1
LAICA	F551W	551	297	2687	23.7
LAICA	F582W	582	324	2936	23.8
LAICA	F613W	613	320	2940	23.9
LAICA	F644W	644	357	4043	23.8
LAICA	F675W	675	314	4575	23.5
LAICA	F706W	706	332	5668	23.7
LAICA	F737W	737	304	7095	23.5
LAICA	F768W	768	354	8824	23.5
LAICA	F799W	799	312	8992	23.2
LAICA	F830W	830	296	11436	23.2
LAICA	F861W	861	369	10505	22.9
LAICA	F892W	892	303	9044	22.5
LAICA	F923W	923	308	6338	22.1
LAICA	F954W	954	319	5620	21.5
NIR					
OMEGA	<i>H</i>	1216	2163	5169	22.6
OMEGA	<i>J</i>	1655	2191	5055	21.9
OMEGA	<i>K_s</i>	2146	2412	5050	21.4
Detection					
SYNTH	F814W	845	2366	73522	24.5

certainties of ~ 0.03 mag. We will discuss the procedure to refine the photometric zeropoints calibrations via SED-fitting techniques in Section 4.2, in the context of the uncertainties reached by the photometric redshifts.

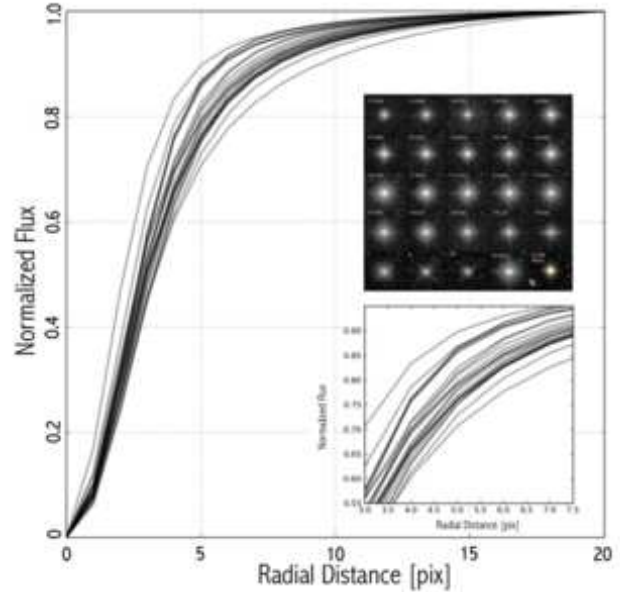


Figure 4. Seeing variability across photometric bands. For a single star, solid black lines represent the scatter in the normalized stellar growth curve as a consequence of the varied PSF across filters (internal top panel). This effect makes the amount of enclosed flux within a fixed aperture to artificially vary, affecting the estimation of accurate photometric colors.

3 PHOTOMETRY

3.1 Multi-wavelength Photometry

As it was thoroughly described in Coe et al. (2005), measuring multicolor photometry in images with different PSFs is not trivial. To perform good quality multi-color photometry, it is necessary to sample the same physical region of the galaxy and to take into account the smearing produced by different PSFs as seen in Fig. 4. We show the distribution of PSFs in the ALHAMBRA survey in Fig. 5, separating among Optical, NIR & synthetic F814W detection images, compressing values from 0.7" to 1.6".

A popular way to proceed is carrying out a PSF-homogenization smoothing the whole dataset to the worst seeing condition, making all images look as they had been taken under the same PSF condition (Labbé et al. 2003, Capak et al. 2007). Even though this methodology immediately defines consistent apertures, the general degradation also implies to sacrifice the quality of the best observations down to the level of the worst. Here we have used *ColorPro* (Coe et al. 2006) which accurately corrects for PSF effects without degrading image quality; Laidler et al. 2007; De Santis et al. 2007 have also developed similar approaches.

To improve the photometric depth and homogeneity, we relied on deep synthetic F814W images (section 3.5) which are ideal for photometric aperture definitions (given its enhanced S/N) and for galaxy morphology estimations.

3.2 PSF-Matched Aperture-Corrected photometry.

ColorPro derives accurate PSF-corrected photometry without degrading high quality images. Initially the software defines every photometric aperture based on the selected detection image. Then it estimates how much encircled flux a galaxy might have missed

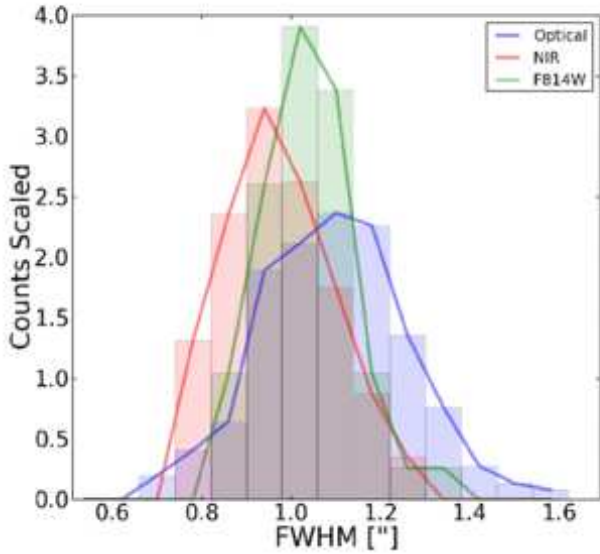


Figure 5. Distribution of seeing conditions for the ALHAMBRA fields. The figure shows the distribution of PSFs (FWHM in arcsec) measured for the Optical images (blue), NIR (red) and synthetic F814W detection images (green). Whereas the most common value for the Optical images peaks at FWHM $\sim 1.1''$, NIR and synthetic F814W detection images does at FWHM $\sim 0.9''$ and FWHM $\sim 1.0''$, respectively.

as a consequence of its PSF by degrading the selected photometry-frame image up to smear other PSF-conditions. The differences in flux measured before and after the degradation are stored and reapplied PSF-correcting magnitudes, as they had all been observed under the same PSF condition. When this procedure runs over the whole dataset, output magnitudes can be easily compared yielding robust photometric colors.

By construction *ColorPro* assumes the selected photometry-frame to have the narrowest PSF and so consistently derive corrections among images. Although desirable, this situation is not always feasible. In the ALHAMBRA-survey synthetic we chose F814W images (Section 3.5) for both source detection (as detection image) and PSF-corrections (as photometry-frame). However sometimes individual filters had a sharper PSF than synthetic F814W images meaning that *ColorPro* was not going to account for those "opposite" differences. To get rid of this situation, we updated the software to automatically degrade those images to match synthetic F814W detection image PSF. To do so we relied on the package PSFMATCH from IRAF (Image Reduction and Analysis Facility). This happened in only few percent of the cases.

SExtractor (Bertin & Arnouts 1996) ISOPHOT apertures produce the most robust colors for faint objects (Benítez et al. 2004) while SExtractor AUTO apertures provide better estimations of galaxy total magnitudes. To encompass the usefulness of both measurements, *ColorPro* defines a photometric transformation which provides both SExtractor ISOPHOT colors and total magnitudes.

Total magnitudes are defined as:

$$M_i = M_i^{ISO} + (M_{det}^{AUTO} - M_{det,i}^{ISO}) \quad (1)$$

while the first term corresponds to the standard SExtractor ISOPHOT magnitude for sources detected on the i^{th} -band, the second term

incorporates the PSF-correction (by applying the photometric differences when degrading the detection image (M_{det}) to the i^{th} -PSFs condition ($M_{det,i}$)). Hence, the second term extends SExtractor ISOPHOT magnitudes into total magnitudes.

Meanwhile ISOPHOT colors are derived as:

$$M_j = M_j^{ISO} + (M_{det}^{AUTO} - M_{det,j}^{ISO}) \quad (2)$$

$$M_i - M_j = M_i^{ISO} - M_j^{ISO} + (M_{det,i}^{ISO} - M_{det,j}^{ISO}) \quad (3)$$

where resulting $M_i - M_j$ colors are just the combination of their SExtractor ISOPHOT magnitudes plus a second term including their relative PSF-corrections. As expected, those cases with equal PSF the second term might be cancelled out providing colors directly from the SExtractor ISOPHOT magnitudes. For a more detailed explanation, we refer the reader to Coe et al. (2006).

3.3 PSF-models

As required by *ColorPro*, it was necessary to generate PSF-models for each individual image. We used the package *DAOPHOT* from IRAF (Stetson 1987) which uses an hybrid method to compute PSF-models. First, it fits the stars central region by using an analytical function (Gaussian, Lorentzian, Moffat or Penny). Second, the outermost parts (regions connected with the background) are empirical fitted point by point, returning typical residua between stars and models around $\sim 3\%$.

We initially ran SExtractor on each image using a very high threshold ($\sim 100 \times \sigma_{Background}$) to detect only very bright sources. We kept detections classified by SExtractor as point-like sources and with *CLASS_STAR* > 0.9 . When representing the magnitude vs the FWHM for those selected objects, we observe they are located in the region of the brightest and most compact sources (Section 3.6.1). To avoid both the very bright sources (mostly saturated stars) and the very faint ones (possibly misclassified galaxies), we selected detections with magnitudes in between $16 < m < 22.5$, yielding a final sample of hundredth of stars per image.

Afterwards, we visually rejected stars with contaminating neighbors and generated mosaic-like images (Fig. 6). This images dramatically decreased the computational time required by *DAOPHOT* to model the PSF. Finally the PSF-models were normalized in flux.

Among the different analytical models considered by *DAOPHOT*, the most recurrent one was the Penny2 profile. This model consists on a Gaussian-like function but with Lorentzian wings, indicating that photometric uncertainties could not be exactly Gaussian. Although typical residuals for PSF models from CCD1, CCD2 and CCD4 are around 3%, CCD3 shows a different behavior with systematically larger residua around 5-10%. This different behavior was probably due to the differences in the efficiency of this detector (CCD3), which was not science grade and significantly worst than CCD1, CCD2 and CCD4 (Cristobal-Hornillos et al. 2013, in prep.).

3.3.1 PSF-Model verification.

We systematically verified each PSF model. First we compared its FWHM with the registered seeing (from the image header) and with

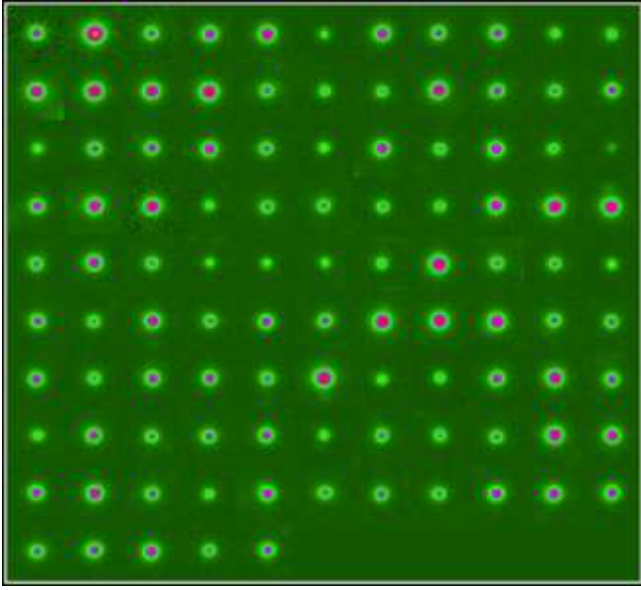


Figure 6. Stars selection. Several hundred of non saturated and well-isolated stars were interactively selected across the images, to derive the PSF models. These selections not only served to assure the fidelity of the resulting PSFs but also to dramatically reduce the computational time required by *DAOPHOT* to generate the models.

the mean FWHM value for the stars used to derive the model. The observed scatter among PSFs does not exceed 3-5%, ensuring that stars and models are well in agreement.

Then the PSF stability among CCDs was also checked out. As introduced in Section 2.2, given the spatial configuration of the LAICA optical system, the four CCDs simultaneously imaged (almost) the same part of the sky under same atmospheric conditions and passbands. This fact made possible to perform statistical comparisons among detectors. Once again we observed good agreements among CCD1, CCD2 and CCD4 but a larger deviation for CCD3 close to a 5-10%.

Finally we studied the radial PSF variability across images to assure the usage of a single PSF-model per image. We defined a new reference system linking every detection (from each CCD) to the center of the telescope’s focal plane. In Fig. 7 we show the dependence of the FWHM as a function of the radial distance for $\sim 20,000$ stars, finding a variation smaller than 5%.

3.4 Simulations.

We designed a set of simulations to test the accuracy of *ColorPro* retrieving precise photometry, across images with varied PSF. The main idea was to degrade a better resolution image to the typical condition of ALHAMBRA (in terms of PSF and background noise) and run *ColorPro* on it expecting retrieve null colors (equal magnitudes) for a sample of galaxies when observed under different PSFs.

We created a mosaic image by rearranging four HST/ACS F814W images from the COSMOS-survey (Scoville et al. 2007) that overlap the ALHAMBRA fields. We rescaled the mosaic to the ALHAMBRA pixel size (from the ACS 0.065 ″/pix to the LAICA 0.221 ″/pix), convolved with ~ 200 PSFs randomly drawn from our

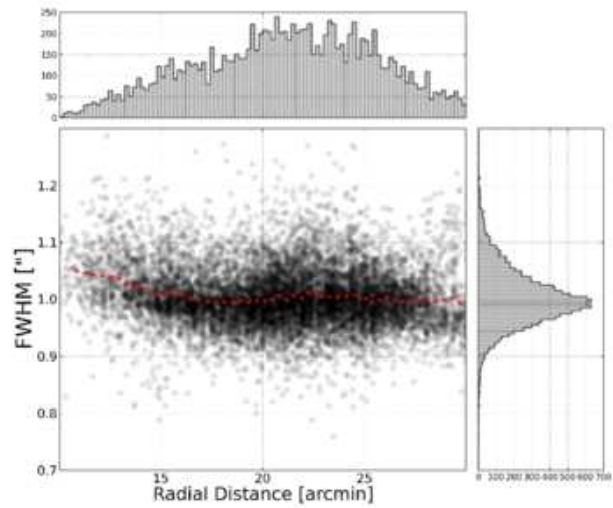


Figure 7. Radial PSF variability across images. The figure shows the radial dependence of the PSF (expressed in arcsec and referred to the primary mirror telescope) for the compilation of stars used to derive the PSF models. The mean value of the distribution (dashed red line) has a scatter smaller than 5% enabling the usage of a single PSF model per image.

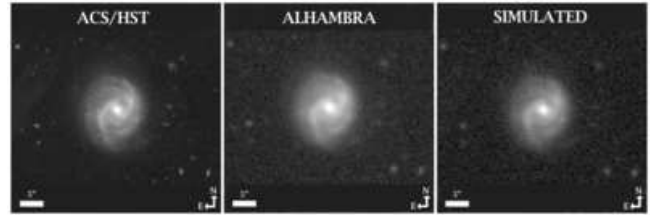


Figure 8. Example of the simulated dataset reproducing the typical observational conditions of the ALHAMBRA images (section 3.4). From left to right, it is shown a galaxy as observed in the ACS/HST image, in the ALHAMBRA synthetic F814W detection image and in the rescaled + PSF degraded + background reapplied ACS/HST image.

models and reapplied background noise using typical values for the ALHAMBRA fields (empirically measured as explained in Section 3.7). An example of the simulated images is shown in Fig. 8 where a galaxy is compared in the ACS/HST image (left panel), in the ALHAMBRA image (middle panel) and in the simulated image (right panel).

3.4.1 Reliability.

We ran *ColorPro* on the new set of ~ 200 mosaics, using the same configuration used for the ALHAMBRA images. We excluded all the detections with photometric problems reported by *SExtractor* (*SExtractor_Flag* > 1) to eliminate several ghosts and other artifacts (trails) within the original images.

We found that the simulated colors showed a dispersion of $\sigma \sim 0.03$ for sources brighter than magnitude F814W = 23.0 and a $\sigma < 0.05$ for sources with magnitudes in between $23 < \text{F814W} < 24$, with negligible biases, as seen in top panel of Fig. 9. The result is in agreement with the expected uncertainties arising from the photometric noise, showing that *ColorPro* is capable to perform accurate PSF-corrections for the ALHAMBRA-like data.

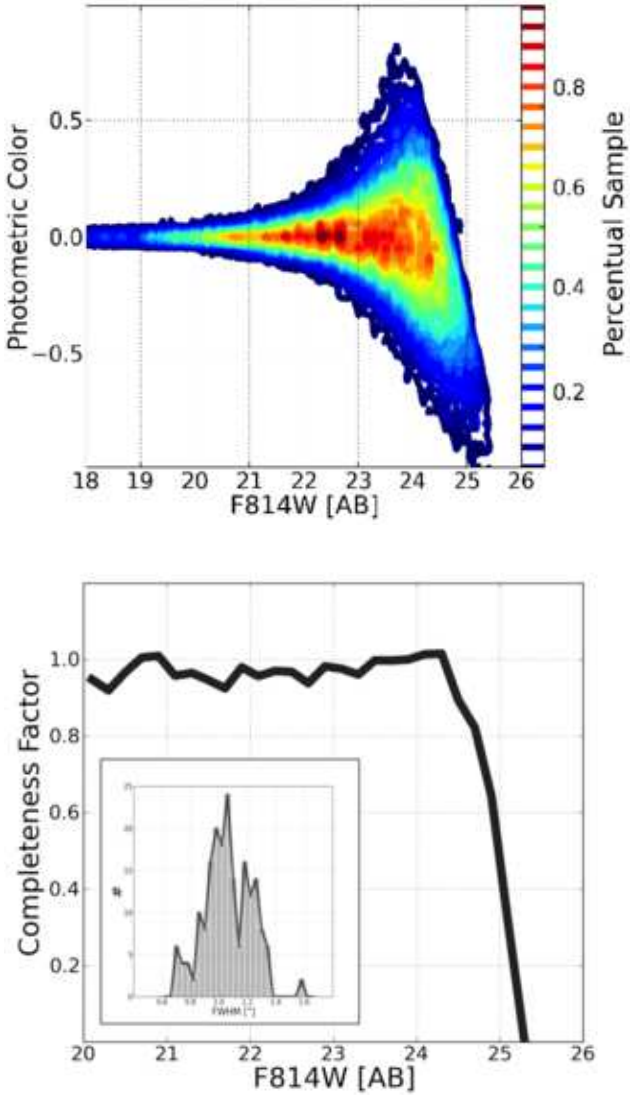


Figure 9. PSF-corrected photometry verifications. We designed a set of simulations (Section 3.4) to estimate both the reliability of ColorPro deriving PSF-corrected photometry and the expected completeness in our images. Top panel shows how ColorPro successfully retrieved null colors (same magnitudes) across simulated images, with a dispersion below 3% for magnitudes brighter than $F814W=23.0$ and 5% for magnitudes in between $23 < F814W < 24$. Bottom panel shows the expected completeness as a function of $F814W$ magnitude.

3.4.2 Completeness.

We studied the expected photometric completeness for the ALHAMBRA fields given by the quality of its images in terms of PSF and background level. For this purpose, we used the previous simulations to derive the statistical probability of detecting a sample of faint galaxies when observed through the typical ALHAMBRA observational conditions. In the bottom panel of Fig. 9 we show the expected fraction of missed galaxies per magnitude range and square degree. The result indicates that ALHAMBRA is photometrically complete down to a magnitude of $F814W \sim 24$. For fainter magnitudes, the number of detections decreases rapidly with a percentage of missed galaxies with magnitude $F814W > 25$ of $\sim 40\%$.

3.5 Synthetic F814W detection images.

In photometric surveys it is a common practice to stack good quality images in order to generate the deepest possible detection images. To define a constant and homogeneous window for all ALHAMBRA fields, we generated synthetic $F814W$ images as the combination of individual bands. To properly calculate the color transformations we used a population of galaxies with typical redshift, magnitude and spectral-type and solved the system of equations generated when estimating the correspondence between synthetic magnitudes among the different filters (eq. 4). As the number of equations (given by the number of galaxies Ng) was substantially larger than the number of degrees of freedom (coefficients), the final equation yielded a dispersion smaller than 1%.

The system of equations among filters for the Ng galaxies is defined as follows:

$$F814W = \langle F814W_{i=1,Ng} \rangle = \sum_{j=1}^{Nf} a_{i,j} \times m_{i,j} \quad (4)$$

An example of the so-derived synthetic $F814W$ images is shown in Fig. 10.

$$F814W = 0.105 \times F706W + 0.178 \times F737W + 0.179 \times F768W + 0.142 \times F799W + 0.115 \times F830W + 0.119 \times F861W + 0.073 \times F892W + 0.049 \times F923W + 0.040 \times F954W \quad (5)$$

Given that the typical error in the individual bands is 2-3%, total zeropoint error in the $F814W$ image is very small, providing high homogeneity. To verify the calibration of the synthetic $F814W$ images, we performed a photometric comparison with the COSMOS field. To reproduce the same photometric measurements as in Ilbert et al. (2009), we ran SExtractor using fixed circular apertures of $3''$. We retrieved ~ 10800 common sources with ALHAMBRA compressing magnitudes from $19 < F814W < 25.5$. The photometric comparison is shown in Fig. 11.

We did not observe photometric zeropoint offsets or trends with magnitude down to magnitudes $F814W < 23.5$. For sources fainter than $F814W = 24.0$ an increasingly dependence on the magnitudes is observed as a consequence of the rapidly decreasing S/N for the ALHAMBRA detections. In an effort to extend the accuracy of the ALHAMBRA photometric measurements, we derived a magnitude-dependent correction to make ALHAMBRA magnitudes reproduce the COSMOS estimations for fixed apertures of $3''$. These corrected magnitudes are included in the final catalogues are explained in the appendix C.

As a separated test, we ran SExtractor on both ACS/ $F814W$ and synthetic ALHAMBRA/ $F814W$ images separately with the same SExtractor configuration. This analysis provided a characterization of the differences in the retrieved detections among both images. For detection magnitudes $19 < F814W < 23.5$ only few tens of sources per CCD were missing from the synthetic ALHAMBRA/ $F814W$ images. Detections fainter than magnitudes $F814W = 23.5$ showed a increasing distribution of undetected sources peaking at a magnitude $F814W \sim 25.5$ where ALHAMBRA is beyond its photometric completeness limit.

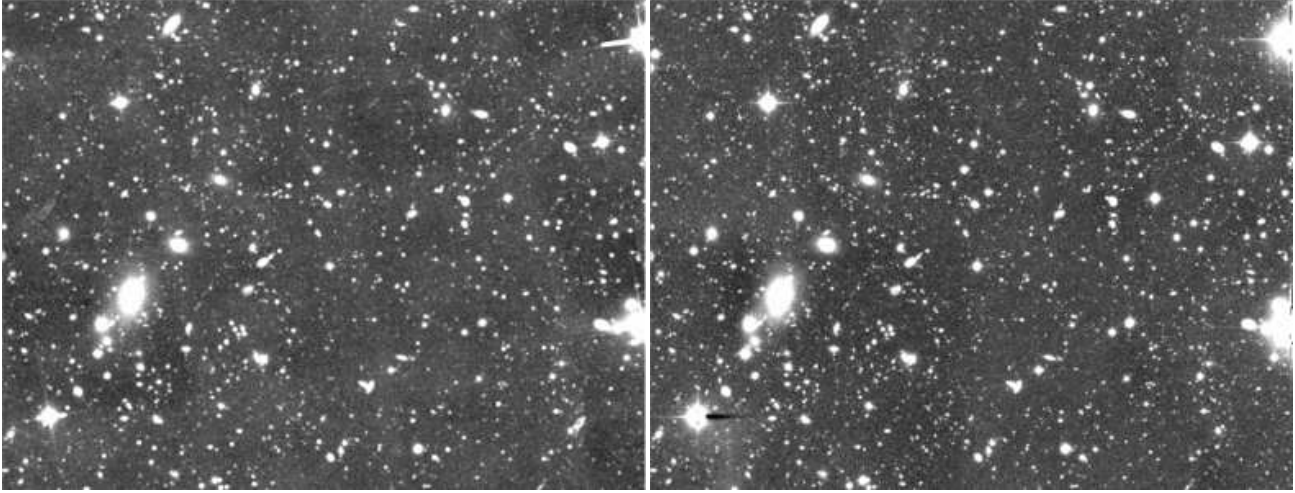


Figure 10. Example of the synthetic F814W images derived for the ALHAMBRA fields. Left panel shows how the original HST/ACS F814W image looks like after been scaled to the ALHAMBRA pixel size, convolved with the ALHAMBRA PSF and photometric noise reapplied. Right panel shows the synthetic ALHAMBRA F814W detection image.

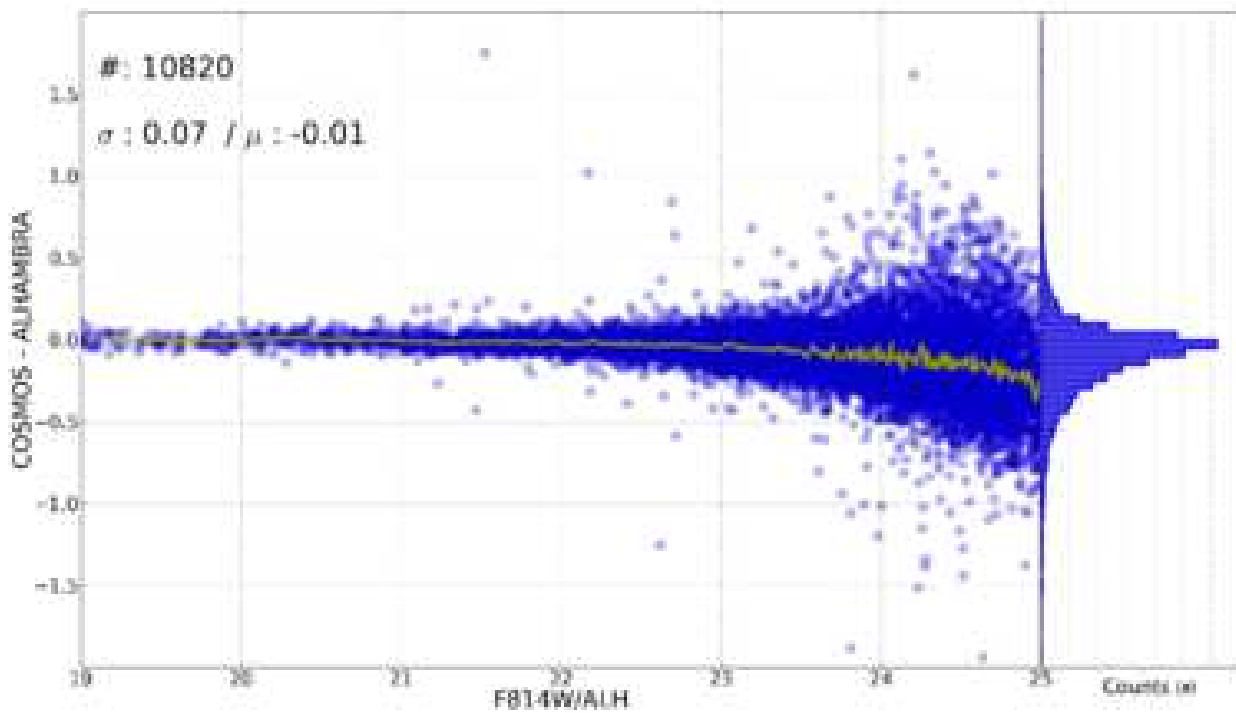


Figure 11. Photometric comparison between the F814W/COSMOS and the synthetic ALHAMBRA/F814W images. In order to reproduce the same photometric measurements as done by Ilbert et al (2009), we ran SExtractor on the synthetic ALHAMBRA/F814W images using fixed circular apertures of $3''$. Selecting a common sample of ~ 10800 detections between ALHAMBRA and COSMOS, we did not find neither photometric zeropoint offsets nor significant bias for detections with magnitudes $19 < F814W < 23$. For sources fainter than $F814W = 23.0$, an increasingly dependence on the magnitude is observed as a consequence of the rapidly decreasing S/N for the ALHAMBRA detections. To make the ALHAMBRA detections to reproduce the COSMOS magnitudes for fixed apertures of $3''$, we derived a magnitude-dependent correction which is included in the final catalogues, as explained in Section 5.

3.5.1 Masks.

In order to improve the source detection efficiency, we masked every saturated star, stellar spike, ghost and damaged area. Initially we ran SExtractor on each synthetic F814W detection image with a special configuration to detect just very bright and ex-

tended sources. We visually checked the extracted sources to exclude any possible nearby galaxy. Then we convolved the resulting SExtractor segmentation maps with a Gaussian function to broaden the previously defined apertures and so remove residual contributions from stellar halos. We repeated the same procedure on the inverse image to deal with negative extended regions generated by

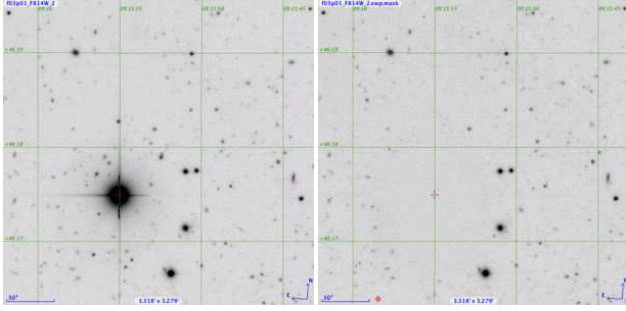


Figure 12. Star masking. In order to improve both the photometric depth and the photometric measurements, F814W detection images were masked out purging saturated stars, spikes, ghosts, negative areas or other artifacts from the images. Figure shows an example about how a saturated star from the original image (left panel) disappears after replacing all its pixels with background signal (right panel).

saturated stars. We combined both positive and negative segmentation maps, defining the total region to be masked out. Finally, we replaced all flagged pixels with background noise to minimize the variation of the image RMS. An example of the masking procedure for a saturated star is shown in Fig. 12.

3.5.2 *SExtractor configuration.*

Assuming an expected variability in terms of PSF (and therefore in photometric depth) among the F814W detection images, we explored the optimal SExtractor configuration which maximizes the number of real detections. For non crowded fields, the most relevant parameters are the minimum number of contiguous pixels *DETECT_MINAREA* and the threshold that the signal has to overpass to be considered a real detection *DETECT_THRESHOLD*.

As the background should in principle have a symmetric structure in Gaussian limit, a similar amount of spurious detections are expected to be retrieved on both sides of the image. Based on this idea, we initially fixed the *DETECT_MINAREA* as twice the image FWHM. Then we studied the lowest threshold that reported the maximum fraction of real detections. We ran SExtractor on the direct image and on the inverse image, hence retrieving the relative fraction of fake over real detections per threshold interval. Finally we chose the threshold value that reported no more than 3% of spurious detections, as illustrated in Fig. 13. In the Appendix D, we show an example of the typical configuration used to perform source detections.

3.5.3 *Flag Images.*

In order to be able to quantify the survey effective area, we generated *FLAG* images for each individual CCD where all problematic pixels were set to 0. As the effective exposure time rapidly decreases when approaching to image edges, we defined homogeneous areas where all sources were adequately exposed (non necessarily detected) in all the 23 bands. We normalized individual weight maps to the maximum exposure time and then flagged the regions with a relative exposure time below the 60% (mostly composed by the image edges).

Meanwhile, these images incorporated the stellar mask infor-

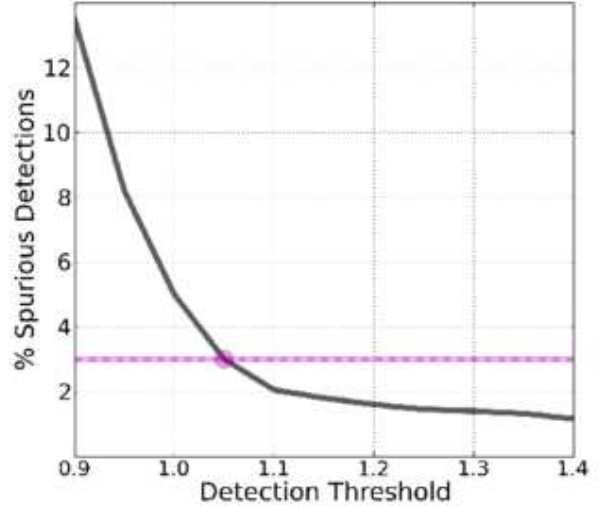


Figure 13. Detection threshold. We studied the lowest SExtractor detection threshold that reported the maximum number of real detections. We initially fixed the *DETECT_MINAREA* as twice the image FWHMW and then ran SExtractor twice (once on the direct and once on the inverse image) retrieving the fraction of fake over real detections as a function of *DETECT_THRESHOLD*. We set the threshold to the value that reported no more than 3% of spurious detections.

mation (Section 3.5.1) as masked regions were replaced by background noise, so provide no detections and artificially varying the expected density of galaxies per unit of area. We combined and stored the information from both criteria in the flag images. Therefore we computed the effective area for each F814W detection image as the direct conversion of the total number of non-flagged pixels into deg^2 , as shown in Table D2. Including all the forty-eight F814W detection images we find a the total surveyed area of 2.79 deg^2 .

3.5.4 *RMS Images.*

As the effective exposure time on an image is position-dependent, detected sources on the edges usually have shorter exposures than sources on the center, therefore generating gradients in the S/N. From a source-detection point of view, as synthetic F814W images were generated as the combination of many filters, occasional inhomogeneities registered on individual *WEIGHT* maps became averaged out. On the contrary, for individual filters (specially for the case of NIR images) we found occasional inhomogeneities across the images (Cristóbal-Hornillos 2013, prep.), artificially biasing the expected photometric depth.

To help disentangle whether a galaxy may be missed on a given filter as a consequence of its intrinsic luminosity (below the detection threshold) or due to an insufficient photometric depth, we used the *WEIGHT* maps (Cristóbal-Hornillos 2013, prep.) to generate a new set of inverseRMS images and define two additional photometric Flags. So, we defined the inverseRMS images by applying the following expression to the *WEIGHT* images:

$$1/\text{RMS} = \sqrt{\text{Weight}} \quad (5)$$

Hence, the *irms_OPT_Flag* and the *irms_NIR_Flag*

Flags indicates to the number of individual bands a detection had a signal in its inverseRMS below the 80%, relative to the maximum value. Therefore, galaxies with large values in these photometric flags (indicating a large fraction of filters photometrically flagged) may provide unreliable photometric redshift estimations.

3.6 Star/galaxy separation.

The star/galaxy classification is a necessary step for accurate extragalactic surveys. Stars as real point-like sources (PLS) are observed as the most compact objects in an astronomical image. However, as detections get fainter (decreasing its S/N) the photometric noise makes progressively complicated differentiating the real morphologies of objects.

We followed a statistical approach to perform star/galaxy separation. We assigned a probability to every detection given its apparent geometry, F814W magnitude, optical F489W - F814W and NIR J - K s colors. For each variable we derived the corresponding probability distribution function (PDF) based on the typical distribution of stars and galaxies. Therefore, every detection is classified in terms of the probability of being a star or a galaxy, as follows:

$$P_{Star} = P_{Star}^{FWHM} \times P_{Star}^{F814W} \times P_{Star}^{Opt} \times P_{Star}^{NIR} \quad (6)$$

$$P_{Gal} = P_{Gal}^{FWHM} \times P_{Gal}^{F814W} \times P_{Gal}^{Opt} \times P_{Gal}^{NIR} \quad (7)$$

$$\text{where } P = P_{Star} + P_{Gal} = 1 \quad (8)$$

Final probabilities are stored on the statistical variable *Stellar_Flag* included in the catalogues. The derivation of the four independent PDFs is now explained.

3.6.1 Geometry and Magnitude.

We used the COSMOS HST/ACS images to explore the star/galaxy selection algorithms, since they are considerably deeper and with a obviously much narrower PSF than the ALHAMBRA dataset.

We ran SExtractor twice, first on the ACS/F814W images and then on the ALHAMBRA/F814W images in single image-mode, representing the detected sources in a FWHM vs F814W magnitude diagram as shown in Fig. 14. We selected detections classified as PLS in the ACS/F814W images and used them to match up the ALHAMBRA/F814W detections.

As seen in Fig. 14 sources brighter than F814W=22.5 classified as PLS on the ACS/F814W images were equally classified as PLS on the ALHAMBRA/F814W (open red circles). However, detections fainter than F814W=22.5 classified as PLS on the ACS/F814W showed progressively larger FWHM values on the ALHAMBRA/F814W. This result sets the ALHAMBRA survey geometrical resolution limit, usable to identify real PLS based on its apparent geometry, to sources brighter than F814W=22.5.

Additionally we investigated the nature of the faint detections appearing as PLS in the ALHAMBRA/F814W images but clearly not belonging to the ACS/F814W PLS sample (green dots). We proceeded reversely by selecting faint F814W>22.5 PLS in ALHAMBRA and matching them to the ACS/F814W detections. The

result showed that those detections were actually very faint extended sources appearing as PLS in the ALHAMBRA/F814W images, where the innermost part was barely detected above the detection threshold due to its low S/N.

3.6.2 Photometric colors.

A popular approach to separate stars from galaxies is based on their spectral differences (Daddi et al. 2004). By combining two photometric colors (one in the optical, one in the NIR) is possible to identify two separated regions where stars and galaxies are typically located, as shown in the left panel of Fig. 15. We initially defined a color-color space generating an optical color as F489W-F814W and a NIR color as J - K s and then, we studied how deep in magnitude this photometric technique applied when considering the level of photometric uncertainties in the ALHAMBRA images.

In order to generate a control sample, we assumed that real PLS (as classified by ACS/F814W images) were all "stars" whereas well extended sources (ES) were assumed to be "galaxies". Considering the resolution of the ACS/HST images and the magnitude range involved in this analysis, the so-derived sample of stars/galaxies represented a good approximation as the expected fraction of misclassified galaxies was actually negligible.

We tested the reliability of this methodology by gradually decreasing the S/N of the sample. Initially we selected only sources with very high S/N (F814W<19) as shown on the left-hand side of Fig. 15. However, as sources get fainter (F814W<23, on the right-hand side) the discrimination among the two classes becomes progressively complicated with ES falling into the initially defined stellar locus and PLS into the galactic Locus.

3.6.3 Stellar flag

Finally, we used the retrieved information from the star/galaxy geometry, F814W magnitude, optical and NIR colors to derive empirical PDFs as shown in Fig. 16. Therefore we assigned a statistical classification to every detection given its observed information. Considering the level of both photometric and geometric uncertainties when deriving the PDFs, we excluded from the classification all detections fainter than magnitudes F814W>22.5 assigning them a *Stellar_Flag* value = 0.5.

We tested the goodness of this statistical classification by comparing the density of selected stars per unit of area. We used the *Trilegal* software (Girardi 2002, 2005) to estimate the expected fraction of stars in the ALHAMBRA fields according to the imaged area, the galactic position and the limiting magnitude. As seen in Fig. 17, we find a good agreement when comparing the statistically derived stellar sample to the *Trilegal* prediction. We observed the ALHAMBRA data to best fit the *Trilegal* estimations when selection as stars all detections with *Stellar_Flag*>0.7

As shown in the right panel of Fig 17, when applying this statistical criteria, we observe that stars dominate the sample down to a magnitude F814W<19. For fainter magnitudes the fraction of stars among galaxies rapidly declines with a contribution of ~1% for magnitudes F814W=22.5. As indicated in the inner right panel, the expected contamination for unclassified stars with magnitudes fainter than F814W>22.5 becomes negligible. We retrieve an averaged stellar density in the galactic halo of ~7000 stars per deg² (~450 stars per CCD) for sources brighter than F814W=22.5.

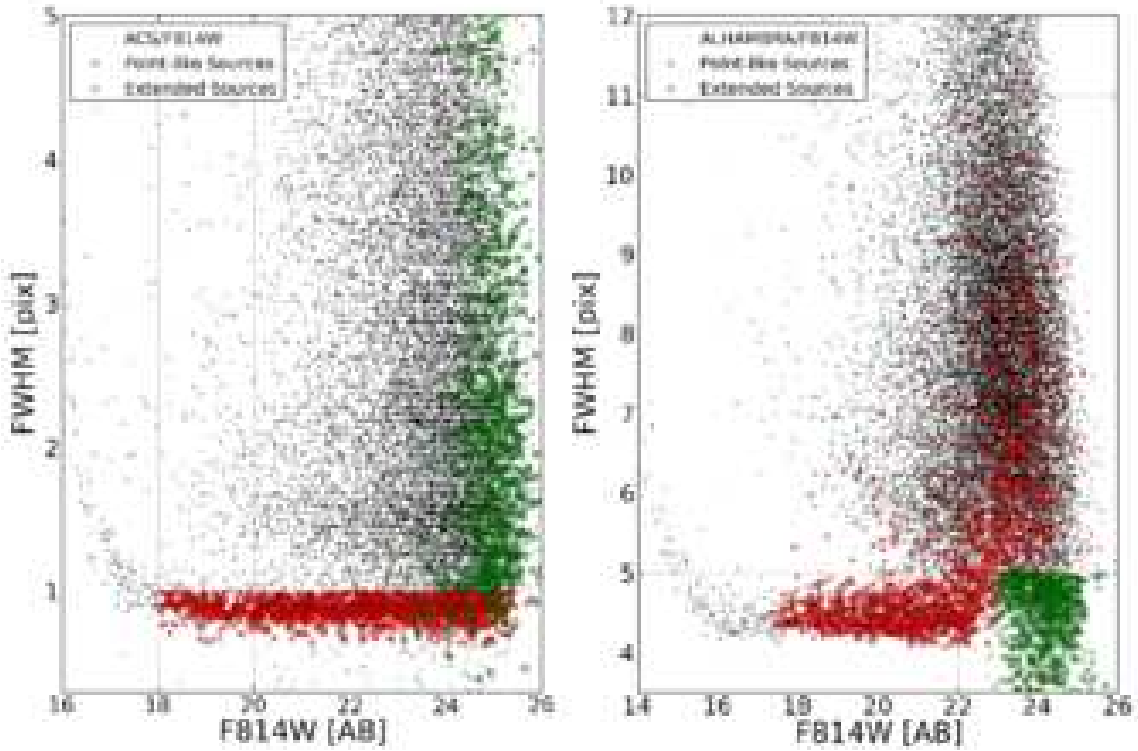


Figure 14. Geometrical distortions. We studied the shape degradation of point-like sources observed in our fields as a function of the apparent magnitude. We used the ACS/F814W images from COSMOS to selected real point-like sources (narrowest FWHM) within the ALHAMBRA fields and so understand how these sources might look like when observed under the ALHAMBRA PSF conditions. As seeing in the figure, detections classified as point-like sources on the ACS/F814W images (red circles) brighter than $F814W=22.5$ were equally classified as point-like sources on the ALHAMBRA/F814W images. However, point-like sources on the ACS/F814W with magnitudes fainter than $F814W=22.5$ showed an increasingly FWHM when observed on the ALHAMBRA/F814W images. This fact indicates the existence of a strong dependency between the accurate geometrical information retrievable from the images and the apparent magnitudes of the detections. Meanwhile we proceeded inversely selecting detections classified as point-like sources in the ALHAMBRA images with magnitudes fainter than $F814W=22.5$ (green circles) and therefore with narrower FWHM that real point-like sources. When observed on the ACS/F814W images, these sources were mostly composed by too faint and extended galaxies where the innermost part was barely detected above the detection threshold due to its low S/N.

3.7 Photometric errors

Image processing (dithering, degradation, stacking, registration, imperfect background subtraction,...) introduces correlations between neighboring pixels making images background noise not describable in terms of a Poissonian distribution. If these effects are not properly taken into account, it can lead to a severe underestimation of the real photometric uncertainties and hence, critically affecting not only the photometric depth estimations (the survey photometric limiting magnitude) but also to the photometric redshift accuracy. Therefore photometric errors have been empirically estimated (following a similar approach as described in Casertano et al. 2000, Labbé et al. (2003), Benítez et al. 2004, Gawiser et al. (2006) and Quadri et al. (2007) to correct for the two main effects.

As explained in Section 3.2, *ColorPro* was updated to automatically degrade every image with a narrower PSF than the detection image. In addition the original NIR images (from OMEGA-2000) were also rescaled to the LAICA pixel size (Cristóbal-Hornillos et al. 2013, in prep.). Both procedures dramatically alter the properties of their original background distributions. More-

over, when deriving photometric uncertainties, SExtractor always assumes the image background to follow a perfect Poisson distribution. This clearly underestimates the noise, as we will see below.

Now we will describe the procedure to derive the empirical photometric uncertainties for each individual image. Initially, we define the separation among real detections and the background signal using the SExtractor segmentation map derived from its corresponding detection image F814W. Every pixel related to a detection is automatically excluded from the analysis. Over the remaining area, we thrown $\sim 50,000$ apertures directly on the images measuring both the enclosed signal and the RMS. The procedure was repeated iteratively spanning a range of apertures between 1-250 pixels. In the meantime, as photometric uncertainties depend on the image total exposure time (which is not necessarily homogeneous), it was necessary to retrieved this information from its corresponding weight maps.

The methodology served to properly estimate the empirical dependence between any galaxy photometric aperture and its RMS. In Fig. 18 we show an example of the typical measured background

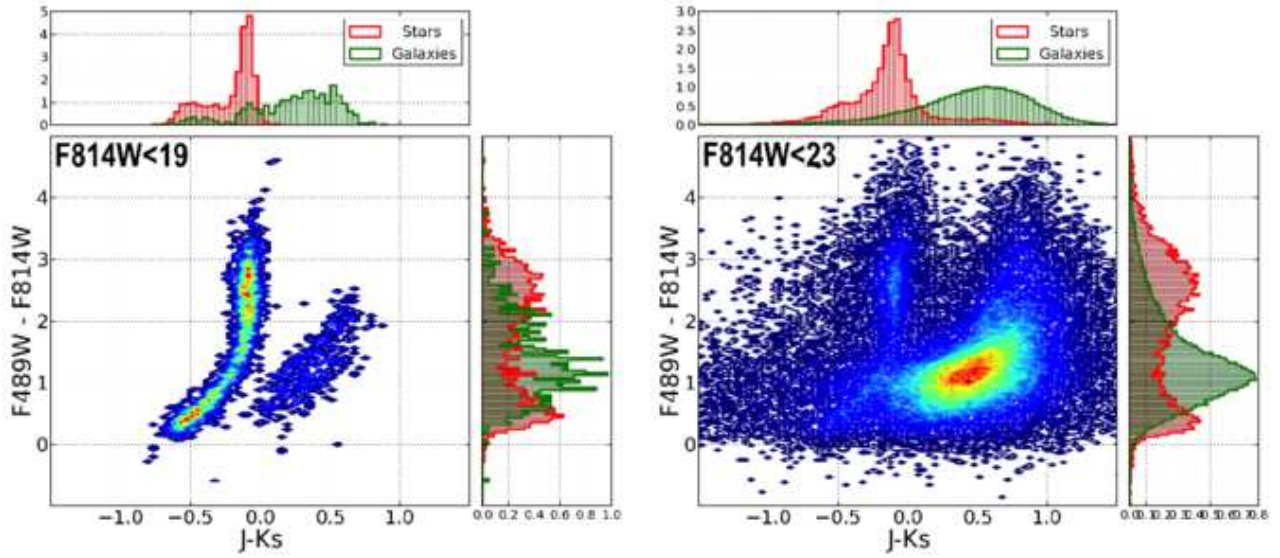


Figure 15. Effect of the photometric uncertainties when discriminating between stars and galaxies. We investigated the possibility of using color-color diagrams to separate stars among galaxies and explored the impact of large photometric uncertainties on it. In order to generate a control sample, we assumed sources classified as point-like sources by the ACS/F814W images to be *stars* and well extended sources to be *galaxies*. Considering the resolution of ACS/F814W images and the magnitude ranges involved, the expected fraction of wrong classified galaxies was actually negligible. As seen in the figure, we defined an optical color as $F489W - F814W$ and a NIR color as $J - Ks$. Whereas for high S/N detections this diagram clearly separated stars among galaxies (left panel), as the S/N declines the photometric uncertainties made the contamination among samples impractical (right panel). Therefore, we decided to apply this methodology only to detections with magnitudes brighter than $F814W = 22.5$.

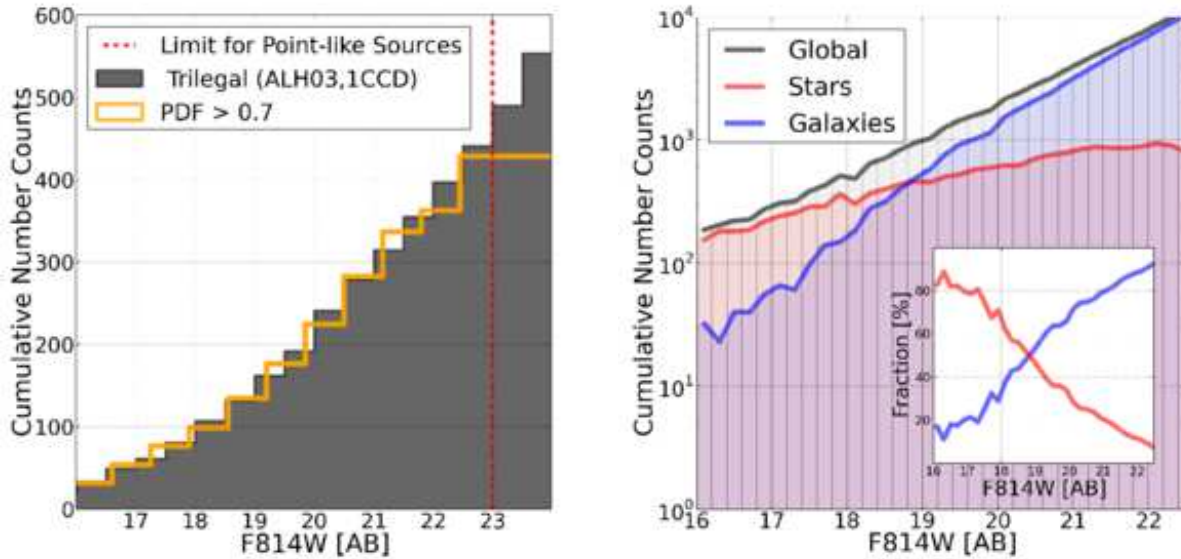


Figure 17. Star number counts. For each field in ALHAMBRA, we compared the number of detections classified as stars based on our statistical criteria (solid yellow line) with that provided by the *Trilegal* software (solid grey histogram), as seen in the left panel. The figure shows an example for a single CCD in the ALHAMBRA-03. We retrieved the best matching among samples when selecting as stars detections with $Stellar_Flag > 0.7$. When applying this statistical criteria to the whole catalogue, we observe stars to dominate the sample down to a magnitude $F814W < 19$. For fainter magnitudes, the fraction of stars among galaxies rapidly declines with a contribution of $\sim 1\%$ for magnitudes $F814W = 22.5$. As indicated in the inner right panel, the expected contamination for unclassified stars with magnitudes fainter than $F814W > 22.5$ becomes negligible. When the analysis is extended to the complete catalogue, we retrieved an averaged stellar density in the galactic halo of ~ 7000 stars per deg^2 (~ 450 stars per CCD), for sources brighter than $F814W = 22.5$.

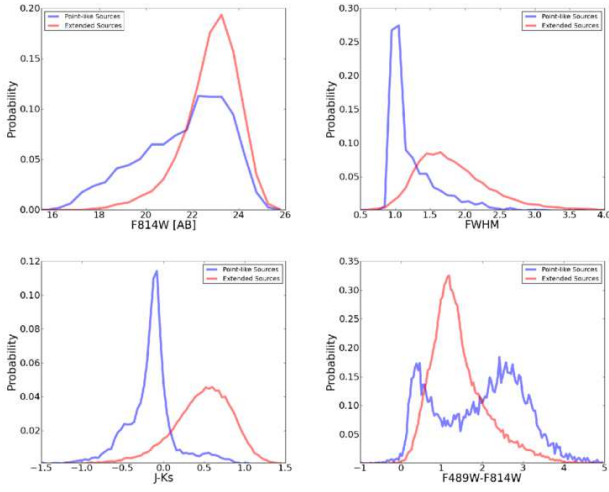


Figure 16. Star/galaxy PDFs. The figure shows the four Probability Distribution Functions derived for a control sample of stars and galaxies selected from the ACS/F814W images. From left to right and top to bottom, the distribution of stars (blue line) and galaxies (red line) as a function of the apparent magnitude F814W, the apparent FWHM, the NIR and Optical colors are shown. These PDFs were used to estimate the probability of a detection to be a star or a galaxy as explained in Section 3.6.3.

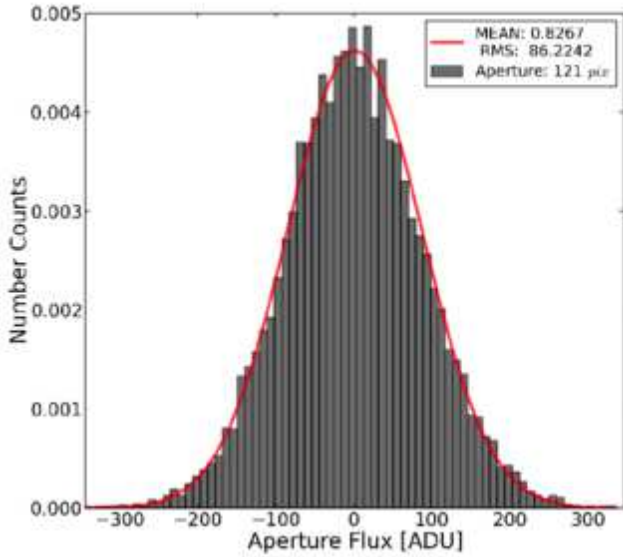


Figure 18. The figure shows an example of the empirically measured background distribution for 121-pixel apertures after drawing $\sim 50,000$ apertures on blank regions. To properly estimate the empirical dependence between photometric apertures and the RMS, the procedure was repeated spanning a range of apertures between 1-250 pixels, so fully covering the expected sizes for the ALHAMBRA detections.

distribution when drawing one pixel apertures. The red line corresponds to the best gaussian fit to the data.

As expected, the ALHAMBRA images are accurately described by a Poisson distribution on small scales. However as apertures become larger, a second term starts dominating the distribution indicating the presence of large-scale correlations among pix-

els. In this case, the background distribution is described by the relation:

$$\sigma(A) = \frac{\sigma_1 \sqrt{N} (C_1 + C_2 \sqrt{N})}{\sqrt{w_N}} \quad (9)$$

where coefficient C_1 indicates the Poisson contribution dominating on small scales, C_2 the contribution on large scales, w_N the corresponding percent weight (from WEIGHT map) and σ_1 the background distribution measured for one pixel apertures.

The relevance of this sort of corrections can be appreciated in Fig. 19 where the differences between a Poisson-based treatment (solid red line) and an empirically estimated (solid black line) are shown. Whereas the left panel indicates the dependence of the expected RMS as a function of aperture size \sqrt{N} , the right panel shows the re-estimated mean photometric uncertainties as a function of magnitude.

3.8 Photometric verification.

As already mentioned in Section 2, taking the advantage that the optical system LAICA was composed by four CCDs which simultaneously imaging (almost) the same portion of the sky under the same atmospheric conditions and passband, it was possible to undertake statistical comparisons among contiguous CCDs.

We performed a systematic comparison between the number of detected sources per magnitude range. As illustrated in the Fig. 20, the results from the four CCDs were highly consistent for magnitudes $F814W < 24$, where ALHAMBRA is photometrically complete. For fainter magnitudes CCD3 showed a decrease in the number of detections, probably due to its poorer efficiency. Meanwhile, we compared the photometric uncertainties between CCDs. Whereas CCD1, CCD2 and CCD4 showed a good agreement, the CCD3 differed from the general trend showing larger photometric uncertainties.

Finally, we did not observe any horizontal shifts among curves indicating no photometric bias at first order. This is illustrated on the right panel of Fig. 20.

4 PHOTOMETRIC REDSHIFTS

BPZ (Benítez 2000) is a SED-fitting method optimized to compute accurate photometric redshifts. Unlike most similar codes, BPZ introduces the use of a Bayesian inference where a maximum likelihood (resulting from a χ^2 minimization between the observed and predicted colors for a galaxy, among a range of redshifts and templates) is weighted by a prior probability. As the resulting $p(z, T)$ is usually a multimodal distribution (with more than one possible peak given the color-redshift degeneracies) the inclusion of any prior information in the analysis serves to eliminate unrealistic solutions reducing the number of catastrophic outliers. In this work, we used an updated version of the code (BPZ2.0, Benítez et al. 2013, in prep.) which includes several changes respect to its original version.

The BPZ2.0 uses a new library composed by five SED templates originally drawn from PEGASE (Fioc & Rocca-Volmerange 1997) but then re-calibrated using the FIREWORKS photometry

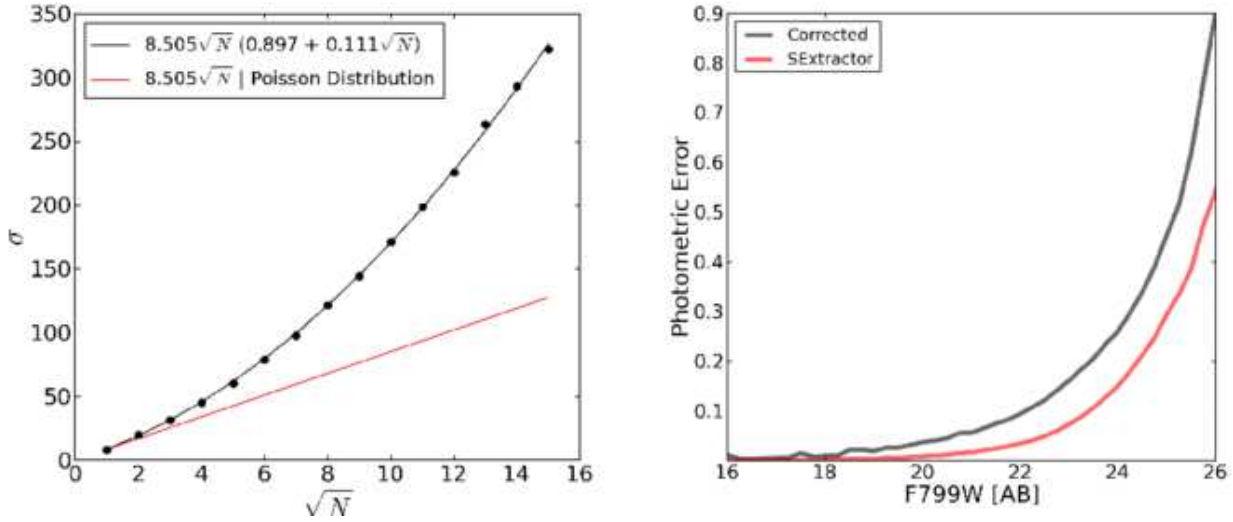


Figure 19. Photometric uncertainties. The figure shows the differences between the photometric uncertainties yielded by *SExtractor* (solid red line) assuming that the background follows a Poisson distribution and those empirically estimated (solid black line) using the methodology described in Section 3.7. Left panel illustrates how the dependence between the RMS and the aperture-size (\sqrt{N}) becomes progressively underestimated by *SExtractor* due to the presence of large-scale correlations among pixels introduced during image processing. As described in equation 9, whereas the number outside the parenthesis in the legend correspond to the background RMS derived for 1-pixel apertures, the numbers inside correspond to the (Poisson) contribution dominating on small scales and to the contribution on large scales, respectively. The right panel compares the average photometric uncertainties, as a function on magnitude, derived by *SExtractor* (solid red line) and using an empirical approach (solid black line). As expected, *SExtractor* always underestimates the real photometric uncertainties, becoming specially significant for faint magnitudes.

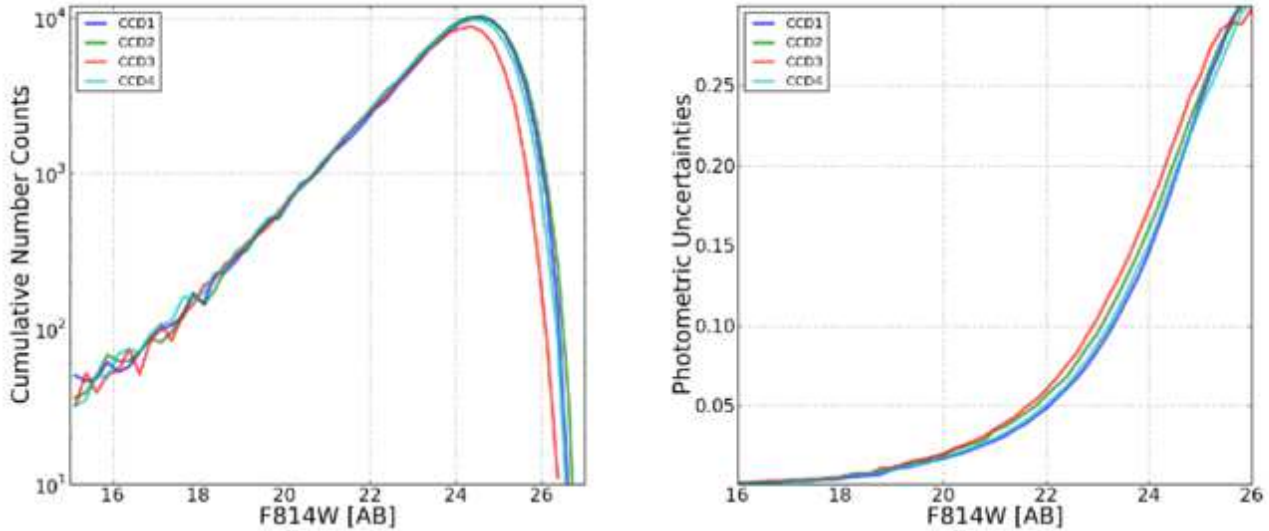


Figure 20. Internal photometric verifications. Using the advantage that the LAICA optical system is an array composed for four CCDs imaging simultaneously (almost) the same regions of the sky, under same atmospheric conditions and under same pass-band, we performed internal photometric checks by comparing statistics from different CCDs. As seen on the left panel, on the one hand, we compared number counts per magnitude range. This analysis served to assure the homogeneity during the detection process. As expected, whereas CCD1, CCD2 and CCD4 are similar, CCD3 behaved slightly worse with a shallower photometric depth. The absence of bumps or horizontal shifts among CCDs indicates homogeneous detections and no problems of any kind with photometric zeropoint offsets, at first order. On the right panel, on the other hand, we compared the photometric uncertainties as a function of the magnitude for the four CCDs. As expected, CCD3 typically showed larger photometric uncertainties than the other CCDs, confirming its poorer performance.

and spectroscopic redshifts (Wuyts et al. 2008) to optimize its performance, i.e., making the templates to have same colors as real galaxies with known redshifts observed with ACS. In addition five GRASIL and one Starburst templates have been added. As seen in the left panel of Fig. 21, this new library includes five templates for elliptical galaxies, two for spiral galaxies and four for starburst galaxies along with emission lines and dust extinction. The opacity of the intergalactic medium was applied as described in Madau et al. (1995). An example of the typical spectral-fitting using the ALHAMBRA photometry is shown in the right panel of Fig. 21. Meanwhile the internal right corner panel corresponds to the resulting redshift distribution function $p(z)$.

The BPZ2.0 includes a new prior which gives the probability of a galaxy with apparent magnitude m_0 having a certain redshift z and spectral-type T . The prior has been empirically derived for each spectral-type and magnitude by fitting luminosity functions provided by GOODS-MUSIC (Santini et al. 2009), COSMOS (Scoville et al. 2007) and UDF (Coe et al. 2006).

In addition, the BPZ2.0 also provides an estimation of the galaxy stellar mass, calculated from the assigned interpolated spectrum of the galaxy by applying the color-M/L ratio relationship established by Kannappan (2007a) to the BPZ templates. For an in-depth discussion, we refer the reader to Benítez et al. 2013, in prep. We performed two different checks to show the robustness of the BPZ stellar masses. First, when comparing the BPZ stellar masses with the masses measured by Bundy (2006a) on the COSMOS field, we observed that the uncertainties are within the expected by their analysis (of about 0.1 - 0.2 dex). On their calibration, they used a Diet-Salpeter IMF while on Bundy (2006a) work they used a Salpeter IMF which explains why our masses are on average 0.09 dex higher than theirs. Secondly, we obtained BPZ stellar masses from a semi-analytical simulation (Merson et al. 2013, Ascaso et al. 2013 (in prep.)) and compared them with the input masses after correcting them by the effect of different IMFs (Bernardi et al. 2010). The mean value of the difference is $\sim 0.13 \pm 0.30$ dex which, as before, is consistent with the uncertainties reported (Mitchell et al. 2013), confirming the reliability of the stellar masses estimations.

Along with the most probable redshift and spectral type for each galaxy, BPZ also provides the *Odds* parameter (Benítez 2000). This parameter is a quality indicator which refers to the integral of the redshift probability within a fixed range ($0.0125(1+z)$, in this case) around the main peak of the $p(z)$ distribution. Therefore, the *Odds* parameter is a measurement of the quality/confidence of the photometric redshift estimation. It is worth emphasizing that the *Odds* makes possible to derive high quality samples with very accurate redshifts and a very low rate of catastrophic outliers. We used a redshift resolution of $DZ = 0.001$ from $0.001 < z < 7.0$. In order to fully cover the spectral-type space, we used an interpolation factor between templates of 7, i.e. expanded the library of templates by generating seven models in between each of the original eleven models. The redshift confidence interval provided by zb_{min} and zb_{max} corresponds to the 68% of the probability distribution function. Note that, in some cases the probability $p(z)$ can go to 0 within this range.

4.1 Photometric redshift accuracy

The normalized median absolute deviation (NMAD) is known to be a robust measurement of the accuracy reached by a sample of photometric redshifts (Brammer et al. 2008). As photometric red-

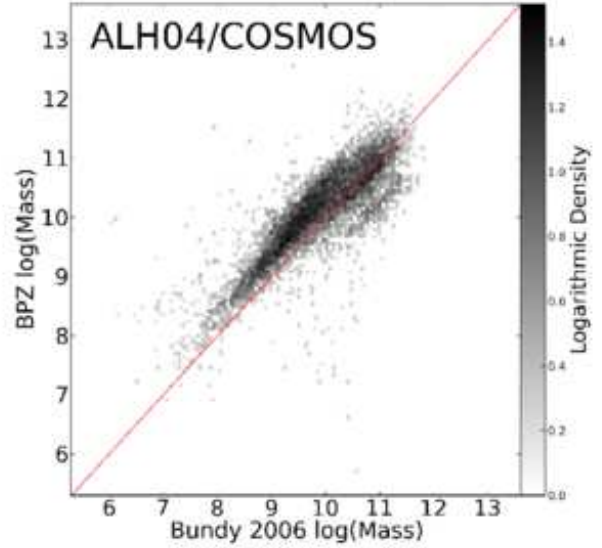


Figure 22. The new version of BPZ provides an estimation of the galaxy stellar mass, calculated from the assigned interpolated spectrum, by applying the color-M/L ratio relationship established by Kannappan (2007a) to the BPZ templates. In the figure, we show a comparison between the BPZ stellar masses with the masses measured by Bundy (2006a) on a sample of galaxies from the COSMOS field. We observe that the uncertainties (of about 0.1 - 0.2 dex) are within those expected by Bundy (2006a).

shifts typically show error distributions with extended tails (departing from a pure Gaussian distribution) along with the presence of several outliers, the NMAD estimator becomes more appropriate than the standard deviation as the former is less sensitive to these long tails and to the presence of catastrophic outliers. NMAD is defined as:

$$\sigma_{NMAD} = 1.48 \times \text{median}\left(\frac{|\delta z - \text{median}(\delta z)|}{1 + z_s}\right) \quad (10)$$

$$\text{and } \delta z = z_b - z_s \quad (11)$$

where z_b corresponds to the bayesian photometric redshift and z_s to the spectroscopic redshift. Along with the scatter it is also important to quantify both the presence of any systematic bias μ and the fraction of catastrophic failures when deriving the galaxy redshift. In this work we established two different definitions for catastrophic outliers:

$$\eta_1 = \frac{|\delta z|}{1 + z_s} > 0.2 \quad (12)$$

$$\eta_2 = \frac{|\delta z|}{1 + z_s} > 5 \times \sigma_{NMAD} \quad (13)$$

As explained in Section 2, ALHAMBRA was designed to partially overlap regions observed by other spectroscopic surveys. We compiled a sample of ~ 7200 galaxies with spectroscopic redshifts to quantify the expected accuracy for the photometric redshift estimations, imposing two strong criteria. On the one hand, we considered only high quality (secure) spectroscopic redshifts.

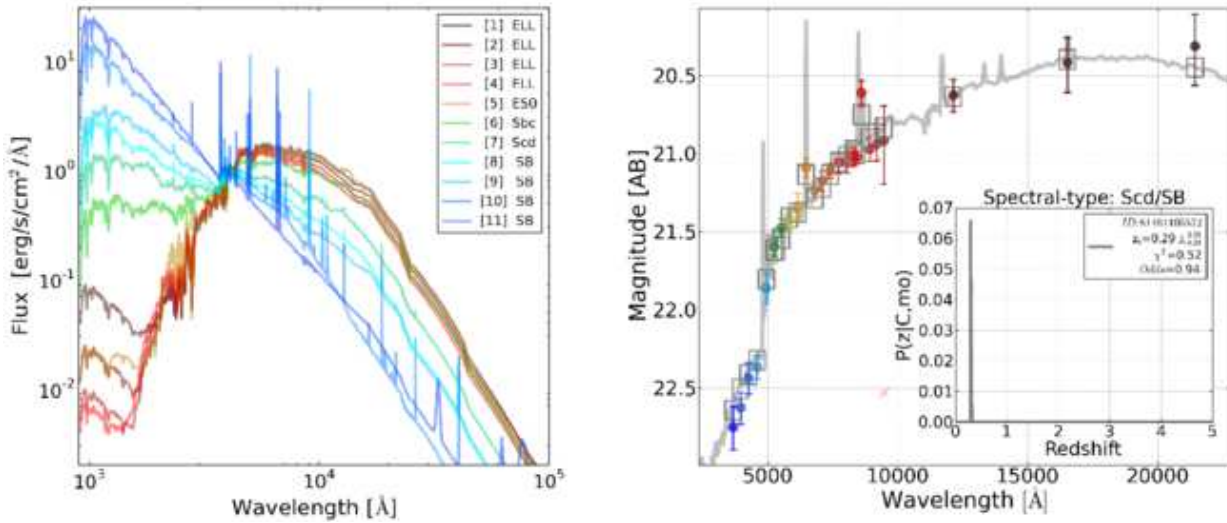


Figure 21. The BPZ2.0 new library is composed by five SED templates originally drawn from PEGASE but then re-calibrated using the FIREWORKS photometry and spectroscopic redshifts to optimize its performance. In addition five GRASIL templates and a SB have been added. In the figure we arbitrarily normalized the SEDs to 4000\AA for an easy visualization. The numerical notation for the BPZ templates used in the catalogues is indicated in the legend. The right panel shows an example of the typical spectral-fitting using the ALHAMBRA photometry, where the internal right-corner figure corresponds to its resulting redshift distribution function $p(z)$.

Table 4. Spectroscopic Redshift samples.

#	Survey	Reference	$\langle F814W \rangle$	$\langle z \rangle$
1269	DEEP-2	Koo et al. 1995	22.64	0.92
1291	COSMOS	Lilly et al. 2009	21.36	0.54
1000	GOODS-N	Cooper et al. 2011	22.75	0.83
2977	GROTH	Demian et al. 2011	22.21	0.70
7237			22.24	0.75

Although this condition dramatically reduced the amount of available galaxies (and probably slightly biasing the sample to the brightest galaxies) it reduces the contamination and the fraction of spurious outliers (Fernández-Soto 2001). On the other hand, to reduce the amount of mismatched galaxies, we derived accurate astrometric corrections between samples (to avoid any offset) and then established a maximum matching distance of ~ 3 pixels ($< 0.7''$), as shown in Fig. 23. This maximum separation was manually set for each survey being the distance at which the distribution of matching distances reached its first minimum. As seen in Fig. 24, the compiled redshift sample shows a mean redshift $\langle z_s \rangle \sim 0.77$ and a mean magnitude (based on ALHAMBRA photometry) $F814W \sim 22.3$. In Table 4 the contribution from each survey is specified, indicating the number of selected galaxies, the mean magnitude and redshift.

As seen in Fig. 25, when compared with the spectroscopic sample, our photometric redshift estimations show a dispersion $\sigma_z = 0.0106$ for $F814W < 22.5$ with a fraction of catastrophic outliers $\eta_1 \sim 2.7\%$. For fainter magnitudes $F814W < 24.5$ the accuracy observed is $\sigma_z = 0.0134$ and the fraction of catastrophic outliers $\eta_1 \sim 4.0\%$. The fraction of catastrophic outliers dramatically decreases when selecting a more restricted sample (excluding X-

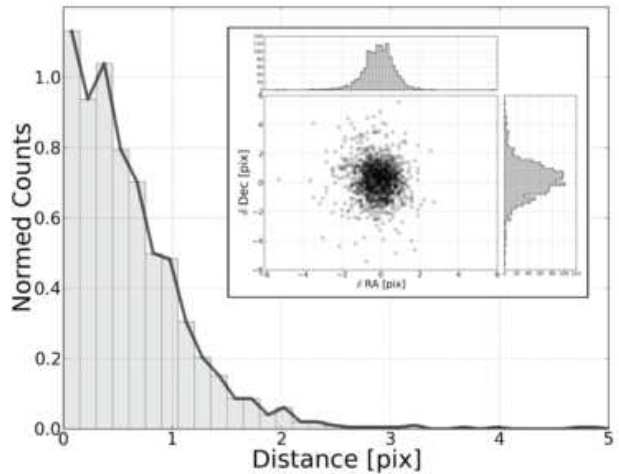


Figure 23. Astrometric matching with spectroscopic samples. In order to reduce the fraction of potential mismatched galaxies, we initially performed second-order astrometric corrections between the ALHAMBRA fields and other surveys, to establish a maximum distance of ~ 3 pixels ($< 0.7''$) to match our detections. This maximum separation was manually set for each survey, being the distance at which the radial matching distribution reached its first minimum. As seen in the main panel, $\sim 60\%$ of the selected spectroscopic sample is well accommodated within a 1-pixel distances. Top right-corner panel illustrates the astrometric dispersion between ALHAMBRA and the overlapping surveys in terms of δRA ($RA^{ALH} - RA^{surv}$) and δDec ($Dec^{ALH} - Dec^{surv}$) in units of pixel.

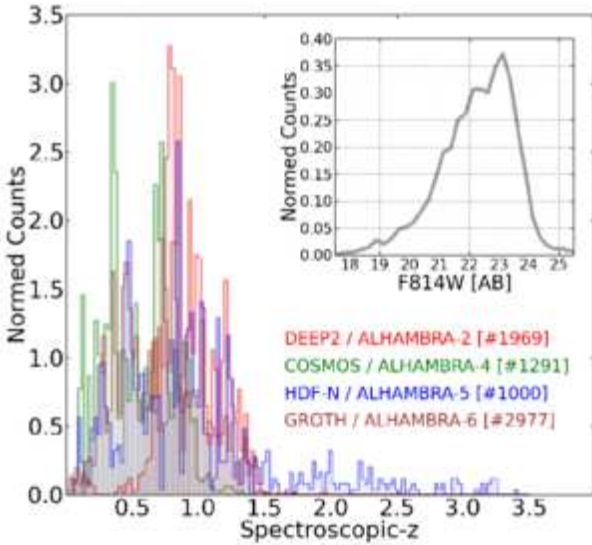
ray emitters, AGNs or detections observed under few bands). In addition, the photo- z error and the fraction of catastrophic outliers rapidly decreases as the *Odds* interval increases. We show the expected accuracy for the photometric redshifts as a function of red-

Table 5. Photometric redshift quality vs spectroscopic redshifts.

Spectroscopic Redshift	σ_z (Odds>0.0)	# (%)	η_1 (%)	η_2 (%)	σ_z (Odds>0.5)	# (%)	η_1 (%)	η_2 (%)	σ_z (Odds>0.9)	# (%)	η_1 (%)	η_2 (%)
$0.00 < z < 0.25$	0.0115	10.8	0.4	0.8	0.0086	3.8	0.1	0.2	0.0056	0.3	0.0	0.0
$0.25 < z < 0.50$	0.0101	21.0	0.6	1.5	0.0087	10.5	0.2	0.4	0.0062	1.6	0.0	0.1
$0.50 < z < 0.75$	0.0136	19.6	1.0	2.4	0.0107	11.5	0.3	0.8	0.0061	1.2	0.1	0.1
$0.75 < z < 1.00$	0.0135	21.4	0.7	2.3	0.0104	12.7	0.2	0.7	0.0066	1.4	0.0	0.1
$1.00 < z < 1.25$	0.0171	13.2	0.4	1.3	0.0125	7.0	0.1	0.4	0.0070	0.3	0.0	0.0
$1.25 < z < 1.50$	0.0194	7.2	0.3	0.9	0.0132	2.3	0.1	0.3	—	—	—	—
$1.50 < z < 1.75$	0.0988	3.4	0.1	0.2	0.0567	0.3	0.0	0.0	—	—	—	—
$1.75 < z < 2.00$	0.1078	1.4	0.2	0.4	0.1620	0.0	0.0	0.1	—	—	—	—

Table 6. Photometric redshift quality vs F814W magnitude.

Magnitude F814W	σ_z (Odds>0.0)	# (%)	η_1 (%)	η_2 (%)	σ_z (Odds>0.5)	# (%)	η_1 (%)	η_2 (%)	σ_z (Odds>0.9)	# (%)	η_1 (%)	η_2 (%)
$18.0 < m < 19.0$	0.0081	0.8	0.0	0.1	0.0073	0.6	0.0	0.0	0.0055	0.1	0.0	0.0
$19.0 < m < 20.0$	0.0083	2.2	0.1	0.3	0.0077	1.7	0.1	0.1	0.0056	0.3	0.1	0.1
$20.0 < m < 21.0$	0.0095	5.3	0.3	0.7	0.0085	4.1	0.1	0.3	0.0059	0.7	0.0	0.0
$21.0 < m < 22.0$	0.0101	11.9	0.4	1.1	0.0093	9.0	0.2	0.5	0.0058	1.3	0.0	0.0
$22.0 < m < 23.0$	0.0140	26.0	0.7	2.1	0.0111	16.0	0.3	0.9	0.0065	1.5	0.0	0.0
$23.0 < m < 23.5$	0.0182	22.8	0.6	2.1	0.0129	9.4	0.2	0.6	0.0045	0.5	0.0	0.0
$23.5 < m < 24.0$	0.0263	30.7	0.9	2.3	0.0118	7.4	0.2	0.4	0.0038	0.3	0.0	0.0

**Figure 24.** Spectroscopic redshift compilation. Given the overlap between the ALHAMBRA fields and other existing spectroscopic surveys, we compiled a sample of ~ 7200 galaxies with secure spectroscopic redshifts to quantify the accuracy for our photometric redshifts. Each survey contribution is color-coded (for visualization) as indicated in the legend. As seen in the figure, the compiled redshift sample mostly covering the ALHAMBRA parameter space, showing a redshift range $0 < z_s < 1.5$ (with a mean redshift $\langle z_s \rangle \sim 0.77$) and a magnitude range (based on ALHAMBRA photometry) $18 < F814W < 25$ (with a mean magnitude $F814W \sim 22.3$).**Table 7.** Photometric redshift accuracy vs Odds for the global sample.

Interval	Sample ¹ (%)	σ_z	η_1 (%)	η_2 (%)
Odds > 0.00	1.00	0.0137	0.04	0.11
Odds > 0.10	0.91	0.0131	0.03	0.09
Odds > 0.20	0.80	0.0123	0.03	0.07
Odds > 0.30	0.71	0.0116	0.02	0.05
Odds > 0.40	0.61	0.0109	0.02	0.04
Odds > 0.50	0.50	0.0102	0.01	0.03
Odds > 0.60	0.36	0.0093	0.01	0.02
Odds > 0.70	0.24	0.0082	0.01	0.01
Odds > 0.80	0.14	0.0069	0.00	0.01
Odds > 0.90	0.07	0.0062	0.00	0.00
Odds > 0.95	0.03	0.0057	0.00	0.00

¹F814W < 24

shift, F814W magnitude and Odds range in Fig. 26. A more detailed analysis can be found in Tables 5 and 6, respectively.

In order to ensure the so-derived $\delta_z/(1+z_s)$ is representative for the spectroscopic sample, the cumulative distribution of sources is represented in Fig. 27. We observed that $\sim 64\%$ and $\sim 90\%$ of the photometric redshifts are well fitted within the formal 1σ and 2σ confidence interval, respectively. This indicates that the uncertainties on z_b are realistic.

4.2 Photometric zeropoint recalibration.

As it was shown in Coe et al. (2006), by comparing the observed colors of galaxies with spectroscopic redshifts against those expected from an empirically defined photo-z library, it is possible to

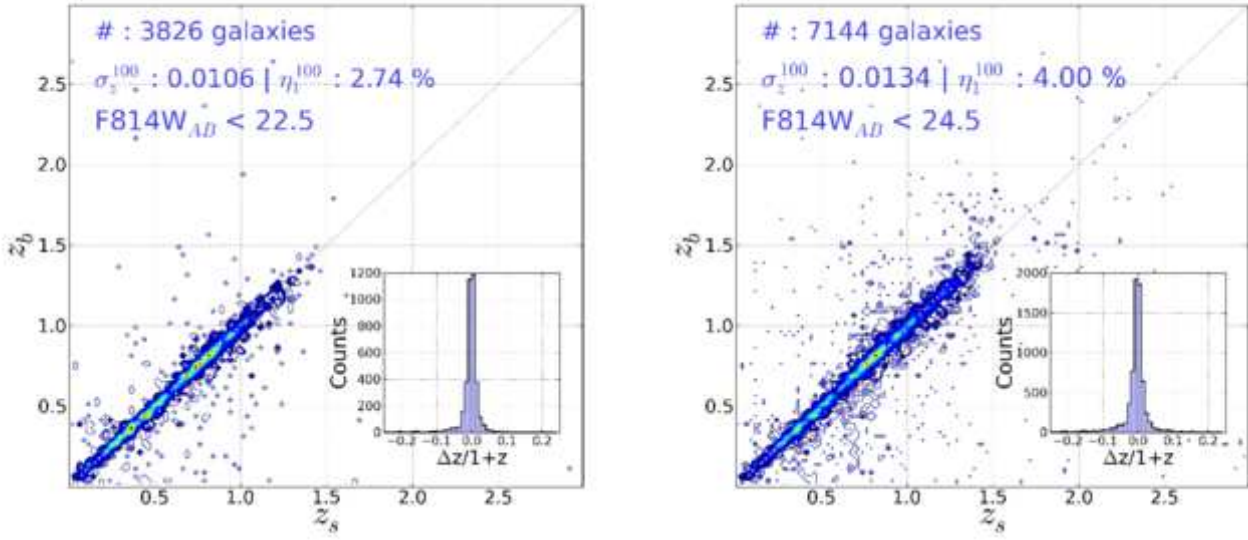


Figure 25. Photometric redshift accuracy. The figures show the comparison between the ALHAMBRA photometric redshifts z_b and the spectroscopic redshifts z_s along with the error distribution $\Delta z/(1+z)$, for two magnitude ranges. While the left panel shows the accuracy obtained for the bright sample ($F814W < 22.5$) with a $\sigma_z < 0.0106$ and a fraction of catastrophic outliers $\eta_1 \sim 2.7\%$, the right panel shows a $\sigma_z < 0.0134$ and a fraction of catastrophic outliers $\eta_1 \sim 4.0\%$ when including the entire sample. In both cases, the fraction of catastrophic outliers (defined in Section 4.1) dramatically reduces when selecting galaxies with higher *Odds*, as indicated in Table 7.

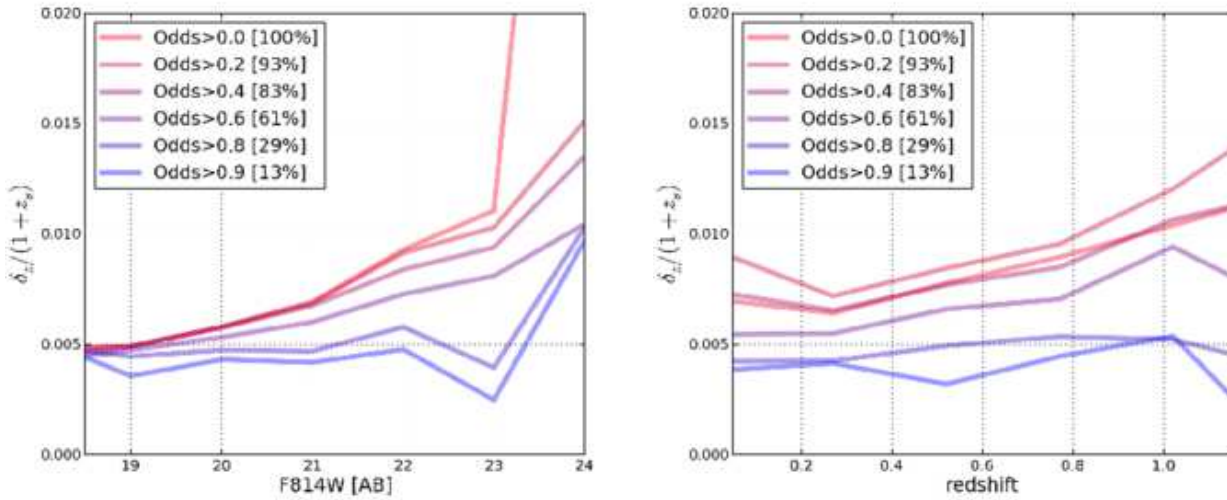


Figure 26. Photometric redshift accuracy as a function of apparent magnitude F814W (left panel) and spectroscopic redshift (right panel). We explored the expected accuracy for our photometric redshifts in terms of a specific magnitude range and redshift range applying different *Odds* intervals.

calibrate photometric zeropoints to within a few percentage, similar or better than the accuracy reached by standard, stellar-based calibration techniques. This capability has been included in the BPZ software package from its initial release (Benítez 2000) and has been applied successfully to several datasets (Capak et al. 2008, Hildebrandt, Wolf & Benítez 2008).

To calibrate the ALHAMBRA zeropoints, we followed this procedure for each individual CCD. First, we selected the spectroscopic redshift galaxies detected in all the 24 bands with a $S/N > 10$,

and chose the BPZ template which best fit its colors at their redshift. We then calculated the ratios between the fluxes predicted in each band by the templates and those observed; the median ratio, which converted to a magnitude represents the zeropoint offset (ZPO) required to match the observed magnitudes to the expected ones. We then corrected the fluxes by this value and iterated until the process converged and the calculated correction was below 1% in all the filters. Since all these changes are relative by nature, the synthetic F814W images were taken as anchor of the whole system.

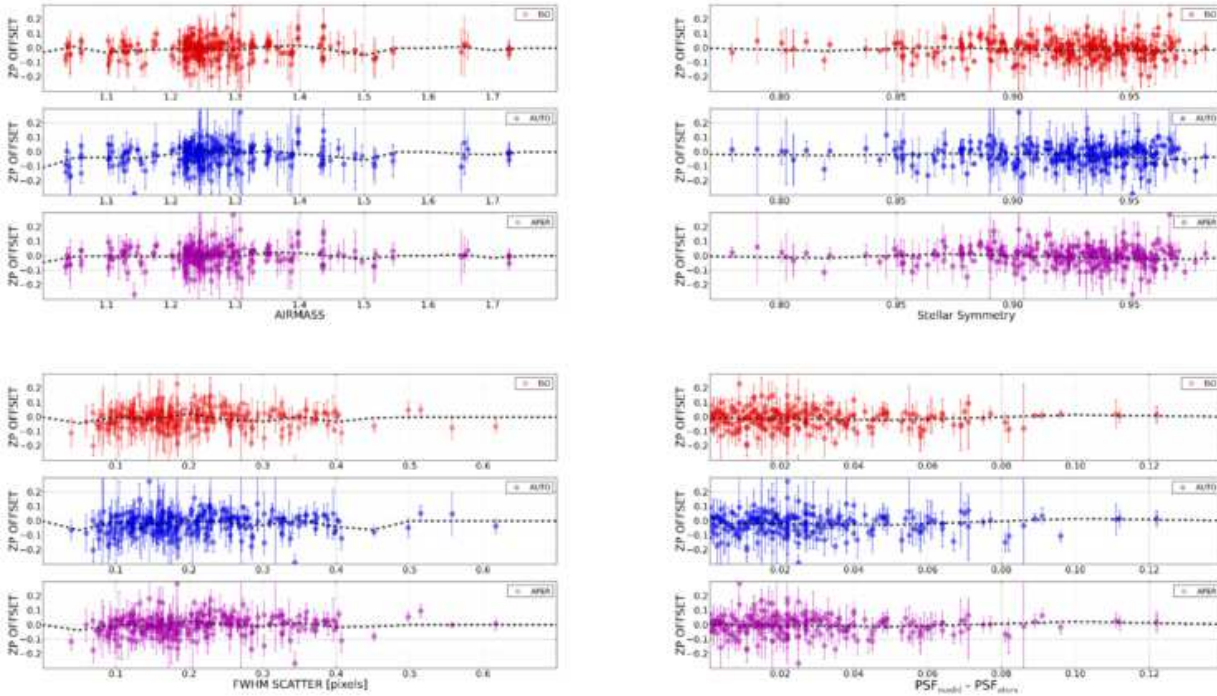


Figure 28. Photometric zeropoint validations. We studied the source of the photometric zeropoint corrections (derived using SED-fitting algorithms) by comparing these quantities with several observational variables. Considering the possibility of a systematic effect during the data reduction, we represented globally the corrections for the ~ 1100 individual images as a function of the AIRMASS (top left panel), the Stellar Symmetry (top right panel), the FWHM Scatter (bottom left panel) & the differences between PSFs-models and stars (top left panel). The procedure was repeated using three different photometric apertures (*SExtractor-ISOphotol* as red circles, *SExtractor-AUTO* as blue circles and *SExtractor-APER* (3") as magenta circles) to discard any systematic effect due to the galaxy sampling regions. As indicated by the mean value of the distributions (dashed black lines), no clear correlations were observed, with fluctuations smaller than 3% (within the expected photometric uncertainties)

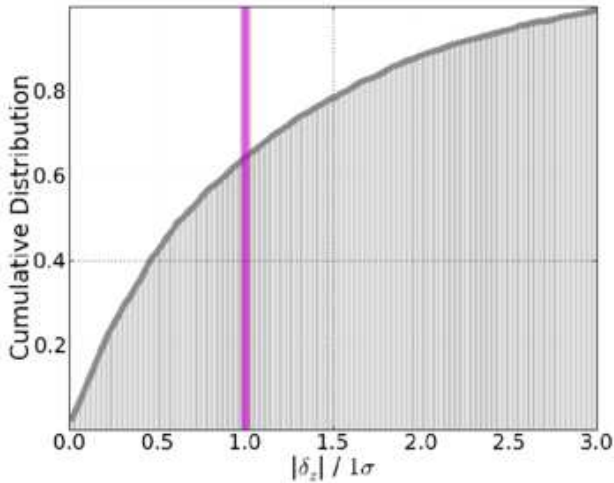


Figure 27. Cumulative Distribution of the ratio $|\delta z|/1\sigma$. We observed that $\sim 64\%$ and $\sim 90\%$ of the photometric redshifts are well fitted within the formal 1σ (magenta vertical line) and 2σ confidence interval, respectively. This indicates that the photometric redshift uncertainties have been reliably established.

Another useful quantity calculated by BPZ is the excess scatter over the expected photometric error, what we call zeropoint error (ZPE). This noise excess can be interpreted as follows. On the one hand, as measurement of the typical mismatch between template and real galaxy colors, averaged over all galaxies observed in that filter. On the other hand, given the flexibility of the template grid, a much more consistent explanation with the observations is that we are just observing a systematic error in the measurement of galaxy colors (to be discussed in Benítez (2013, in prep)). It is essential to include this factor, in addition to the standard photometric error, to produce photo-z estimates significantly more accurate and robust.

We explored the dependence of the amplitude of these zeropoint corrections on several observational variables. As illustrated in Fig. Fig. 28, considering the possibility of a systematic effect during the data reduction, we represented globally the zeropoint corrections for the ~ 1100 individual images as a function of the AIRMASS (top left panel), the Stellar Symmetry (top right panel) defined as the ratio of a/b parameters (Table C1), the FWHM Scatter (bottom left panel) & the differences between PSFs-models and stars (top left panel). The procedure was repeated using three different photometric apertures (*SExtractor-ISOphotol* as red circles, *SExtractor-AUTO* as blue circles and *SExtractor-APER* (3") as magenta circles) to discard any systematic effect due to the galaxy sampling regions. As indicated by the mean value of the distributions (dashed black

[h!]

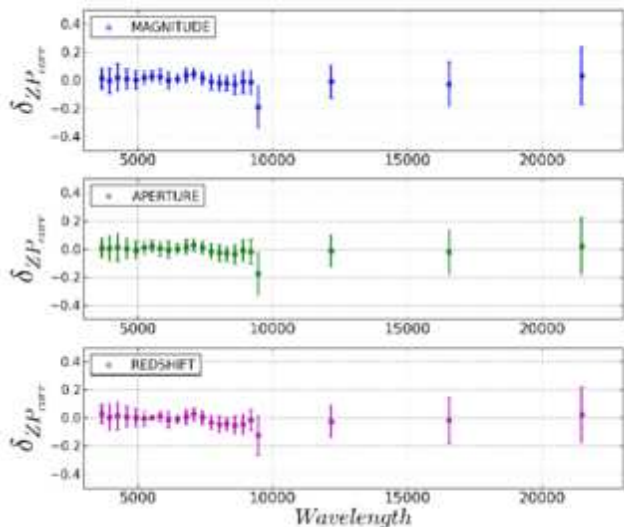


Figure 29. Photometric zero-point validations II. We also studied the robustness of the photometric zero-point corrections using different samples of galaxies and comparing their outcomes. Therefore, we split the spectroscopic sample in equal-sized groups based on its magnitude ($F814W < 22.5$ & $F814W > 22.5$), aperture size ($\text{area} < 125$ pix & $\text{area} > 125$ pix) and redshift ($z < 0.81$ & $z > 0.81$) and derived new photometric zero-point corrections using BPZ. As observed in the figure, for all the three cases, the differences among samples (δ_{ZP}) were always smaller than the internal dispersion given by the error bars. This result reassures that zero-point corrections do not depend on any specific redshift range or spectral-type but probably on the inherent differences between the calibrations obtained from traditional color transformations based on stars and the average colors of galaxies as defined by the BPZ template set, calibrated with HST observations.

lines), we did not observe any clear correlations, with typical fluctuations smaller than 3% (within the expected photometric uncertainties).

We explored whether zero-point offsets depended on the magnitude, i.e. whether brighter galaxies (with larger S/N ratio) would show smaller corrections. Then, we split the spectroscopic sample into two equal-sized groups with galaxies brighter and fainter than $F814W = 22.5$. As seen in Fig. 29 (blue dots) the corrections derived for both samples are the same, within the typical level of photometric uncertainties. Even though filter F954W showed a clear disagreement among samples, its scatter was as large as ~ 0.3 magnitudes indicating other sort of problems perhaps related to the reductions. To look for a dependence on the photometric aperture size, due to some effect related to the PSF corrections we again divided the spectroscopic sample into two equal-sized groups with photometric areas smaller (and larger, respectively) than 125 pixels. As seen in Fig. 29 (green dots) differences among samples were always within the photometric scatter. Finally the dependence between redshift range and zero-point offsets was also considered assuming a possible effect due to evolution in the galaxy populations (since the BPZ templates do not include any evolution). As seen in Fig. 29 (magenta dots) the differences obtained from both samples were smaller than 3% and so within the error bars regime. We therefore conclude that the zero-point offsets do not depend on the

photometric treatment and represent real differences between the calibration obtained from traditional color transformations based on stars and the average colors of galaxies as defined by the BPZ template set, which is based on the colors of galaxies observed with HST.

4.2.1 Photometric ZP calibrations using photometric redshifts.

Although ALHAMBRA was designed to overlap with other spectroscopic surveys, only $\sim 40\%$ of its fields had enough galaxies with spectroscopic redshifts to derive zero-point corrections, as described above. As discussed in Section 4.2 the absence of any clear dependence on the observational parameters made unfeasible any extrapolations among different fields. Given the obvious photometric improvement when applying the zero-point corrections, this fact created a serious problem of inhomogeneity for all those fields without available spectroscopy.

We realized that the photometric redshifts obtained for emission line galaxies were quite robust to changes in the zero-point calibration and therefore we could treat those redshifts as spectroscopic for calibration purposes, obtaining an automatic and self-contained zero-point correction for all our fields. Thus, we ran BPZ on the photometric catalogs with the original, stellar-based zero-point estimations. Then we selected a sample formed by those galaxies observed in all 24 filters, large S/N ($F814W < 23.0$), good fit to the SED ($\text{Odds} \geq 0.9$ and $\chi^2 \leq 1$) and classified by BPZ as late-type galaxies ($tb > 7$). We applied the procedure described in Section 4.2, using the photometric redshifts as spectroscopic values and iterating until convergence was reached. This is basically equivalent to calibrating the ZP using the slope of the continuum of the ELGs.

In the top panel of Fig. 30 we show the photometric redshift accuracy when using three different calibration methods: the original zero-points (red line), corrections derived from photometric redshifts (blue line) and corrections from spectroscopic redshifts (green line). The results indicate that the methodology presented here successfully improved the photometric redshifts accuracy almost up to the level provided by the spectroscopic sample, and it also dramatically reduces the fraction of catastrophic outliers. The bottom panel of the Fig. 30 shows how the corrections derived with late-type galaxies worked very well for early-type galaxies, showing that the corrections were real and independent of the particular choice of templates in the library. It is worth noting that even if the accuracy reached by this method was always slightly worse than that provided by a real spectroscopic sample, it was always much better than the standard stellar-based calibration. Therefore, we decided to apply this kind of zero-point calibrations whenever a spectroscopic sample was not available, which significantly improved the overall homogeneity of the ALHAMBRA sample. This kind of calibration, promises to have wide application to narrow band surveys as JPAS (Benítez et al. 2009)

4.3 Photometric Redshift Distributions

One of the main advantages of ALHAMBRA is that it includes 8 different lines of sight widely separated providing a more realistic estimation of both the typical redshift distribution of galaxies across cosmic time and its inherent variability (cosmic variance).

Considering the probabilistic nature of the photometric redshift estimations, instead of relying on the most likely solution (given by any point estimate) it is desirable to make use of the

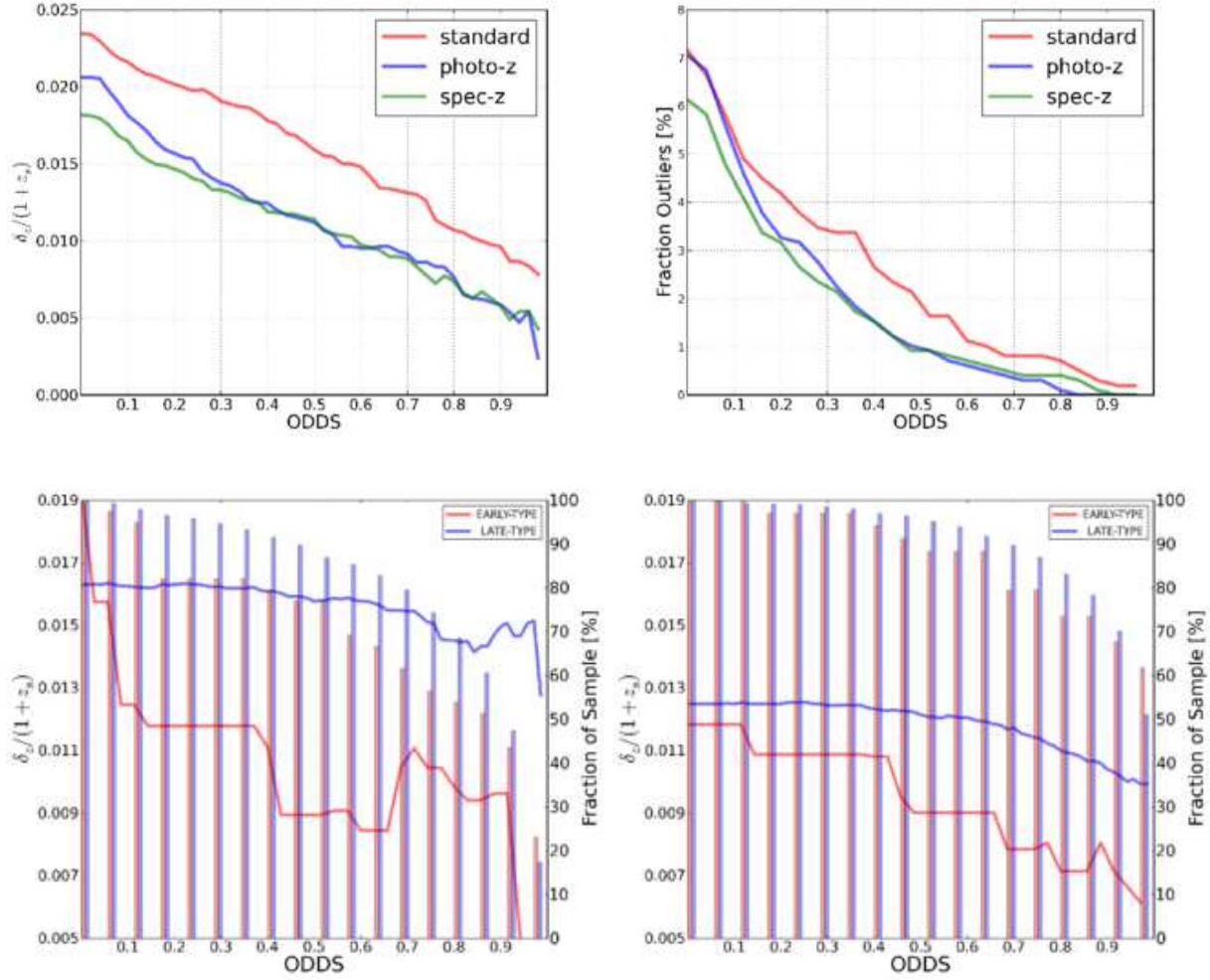


Figure 30. Here we show the feasibility of using emission line galaxies to derive photometric zeropoint corrections. To do so, we used the spectroscopic redshift sample to study the performance of our photometric redshifts (in terms of accuracy and fraction of catastrophic outliers) when applying zeropoint corrections derived from three different approaches: using a standard stellar-based method (red line), using photometric redshifts derived from emission line galaxies (blue line) and using a spectroscopic redshift sample (green line). As seen in the top left panel, photometric redshifts using emission line galaxies not only improved the outcomes using the stellar-based method but also increased its final accuracy up to the level of the spectroscopic method for galaxies with secure photometric-redshift ($Odds > 0.3$). In addition, the fraction of catastrophic outliers was also significantly reduced as shown in top right panel. Meanwhile, we studied the impact of using emission line galaxies (late-type) to calibrate absorption line galaxies (early-type). We compared the performance of both spectral-types separately before (left bottom panel) and after (bottom right panel) applying the zeropoint corrections. As seen in the bottom panels, not only the accuracy for the late-type galaxies (solid blue line) improved significantly with the corrections but also the early-type galaxies (solid red line). Meanwhile, the fraction of galaxies per $Odds$ interval (vertical bars) increased homogeneously among spectral-types, indicating that a larger number of galaxies with secure redshift were found after the calibration.

complete information yielded by the probability distribution functions $P(z, T|C)$ (Benítez 2000, Coe et al. 2006, Mandelbaum et al. 2008; Cunha et al. 2009; Wittman 2009; Bordoloi et al. 2010; Abrahamse et al. 2011; Sheldon et al. 2012). This approach represents a more convenient estimator as the $p(z)$ is not always well represented by a single and symmetric (Gaussian-like) distribution. For most faint galaxies, where the photometric information becomes scarce due to the S/N, redshift probability distributions usually become multimodal and completely asymmetric. In such situations drawing a single value from the distribution represents a clear loss of information or bias. The combination of all $P(z, T|C)$ fully describes the redshift distribution of galaxies indicated by the photometric data.

Therefore, we define the global photometric redshift distribution $P(z)$ as:

$$P(z) = \sum_{i=1}^{N_g} P_i(z) = \sum_{i=1}^{N_g} \left[\frac{\int dT p_i(z, T)}{\int dT \int dz p_i(z, T)} \right] \quad (14)$$

where $p_i(z, T)$ represents the probability distribution function for the i^{th} galaxy over the redshift range z and spectral-types T .

We also ran BPZ on the photometric catalogue used by Ilbert et al. (2009) to derive the global redshift probability distribution function $P(z)$ for the COSMOS field and so consistently compare it with our results. We initially compared the $P(z)$ derived

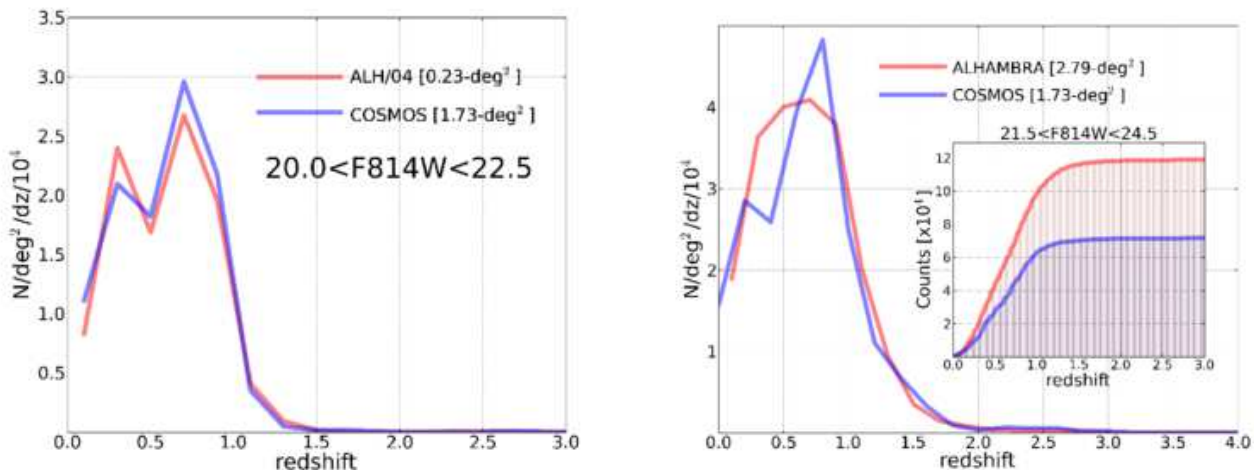


Figure 31. Comparison of the redshift probability distribution function $P(z)$ between ALHAMBRA and COSMOS. Considering the probabilistic nature of the photometric redshift estimations, we relied on the complete information yielded by the $P(z)$ to derive the redshift probability distribution functions for each of our fields. In addition, we ran BPZ on the photometric catalogue used by Ilbert et al. (2009) to derive the $P(z)$ for the COSMOS field and so consistently compare its redshift probability distribution with ALHAMBRA. As seen in the left panel, when comparing the $P(z)$ derived from ALHAMBRA-04 (red line) and COSMOS (blue line) both distributions consistently reproduce a double peak at redshifts $z \sim 0.3$ and $z \sim 0.9$, respectively. However, whereas the ALHAMBRA-4 field shows a mean redshift $\langle z \rangle = 0.60$ for $F814W < 22.5$ and $\langle z \rangle = 0.87$ for $F814W < 25.5$, the COSMOS field shows a mean redshift $\langle z \rangle = 0.66$ for $F814W < 22.5$ and $\langle z \rangle = 0.96$ for $F814W < 25.5$. Meanwhile, the global $P(z)$ derived averaging the seven ALHAMBRA fields shows a mean redshift $\langle z \rangle = 0.56$ for $F814W < 22.5$ and $\langle z \rangle = 0.85$ for $F814W < 25.5$, as seen in the right panel. This result indicates that the COSMOS field shows a clear over-density with respect to the mean value, indicating that the COSMOS field has a rather peculiar redshift distribution which mimics a significant redshift density evolution effect.

using the ALHAMBRA-4 data (red line) with the $P(z)$ derived using the COSMOS data (blue line), as seen in the left panel of Fig. 31, where both distributions consistently reproduce a double peak at redshifts $z \sim 0.3$ and $z \sim 0.9$, respectively. However, whereas the ALHAMBRA-4 field shows a mean redshift $\langle z \rangle = 0.60$ for $F814W < 22.5$ and $\langle z \rangle = 0.87$ for $F814W < 25.5$, the COSMOS field shows a mean redshift $\langle z \rangle = 0.66$ for $F814W < 22.5$ and $\langle z \rangle = 0.96$ for $F814W < 25.5$, as seen in the right panel of Fig. 31. Meanwhile the global photometric redshift distribution derived for all the seven ALHAMBRA fields (excluding stars) shows a mean redshift $\langle z \rangle = 0.56$ for $F814W < 22.5$ and $\langle z \rangle = 0.85$ for $F814W < 25.5$, as seen in the right panel of Fig. 33. This result indicates that as it is known, the COSMOS field shows a clear over-density with respect to the mean value derived averaging the seven ALHAMBRA fields. In fact, the average galaxy number in COSMOS goes up by a 60% between $z=0.4$ and $z=0.7$, whereas no such effect is observed in our average.

To study the evolution of the number counts as a function of the magnitude F814W and redshift, we derived the averaged redshift probability distribution function for the ALHAMBRA fields. As seen in the left panel of Fig. 32, the solid red line corresponding to the mean redshift distribution (per bins of 0.5 mags) indicates a clear evolution moving from a $\langle z \rangle \sim 0.2$ for $F814W < 20.5$ to a $\langle z \rangle \sim 0.8$ for $F814W > 23.0$. Inversely, the right panel of Fig. 32 shows how the peak of the averaged distribution of galaxies increases as a function of the redshift for different magnitude ranges.

We explored the variance in the redshift-magnitude distribution of galaxies as a function of the absolute B magnitude and the spectral-type. As seen in Fig. 34, we split the sample among early-type galaxies (top panel, defined as $1 < T_b < 5$) and late-type galaxies (bottom panel, defined as $7 < T_b < 11$) to compare the re-

sulting distributions among each of the 7 individual ALHAMBRA fields (A_i) + 1 averaged sample (*Global*). As observed from the figure, where the logarithmic density is color-coded, whereas each individual field shows clear and identifiable structures at different redshifts, the global sample shows a much more smooth distribution. In particular, we find that the well-known bimodal distribution in the COSMOS field (A4) is not systematically observed along the other fields. Once again, this result emphasizes the usefulness of the ALHAMBRA sample to measure statistical properties of galaxies.

4.4 Photometric redshift checks.

Applying the same approach as explained in Section 3.8, we performed internal photometric redshifts checks to compare our results among contiguous CCDs. As illustrated in Fig. 35, the statistical results were consistent between CCDs showing a scatter within the intrinsic variance for the sample observed by each CCD.

4.5 Photometric redshift depth

Due to color/redshift degeneracies, it is possible to have galaxies which are detected at high S/N in many filters but for which no univocal redshifts can be derived. One of the main practical ways of characterizing the effective completeness and depth of a photometric redshift catalog is by using the amount of galaxies with *Odds* above a certain threshold, which basically tells us how many galaxies we can expect to have meaningful, univocal photometric redshifts (Benítez 2000, Benítez 2009b).

We therefore took into account the *Odds* to carry out a set of analysis and evaluate the completeness and accuracy of our performance. For this work we set the interval to compute the *Odds*

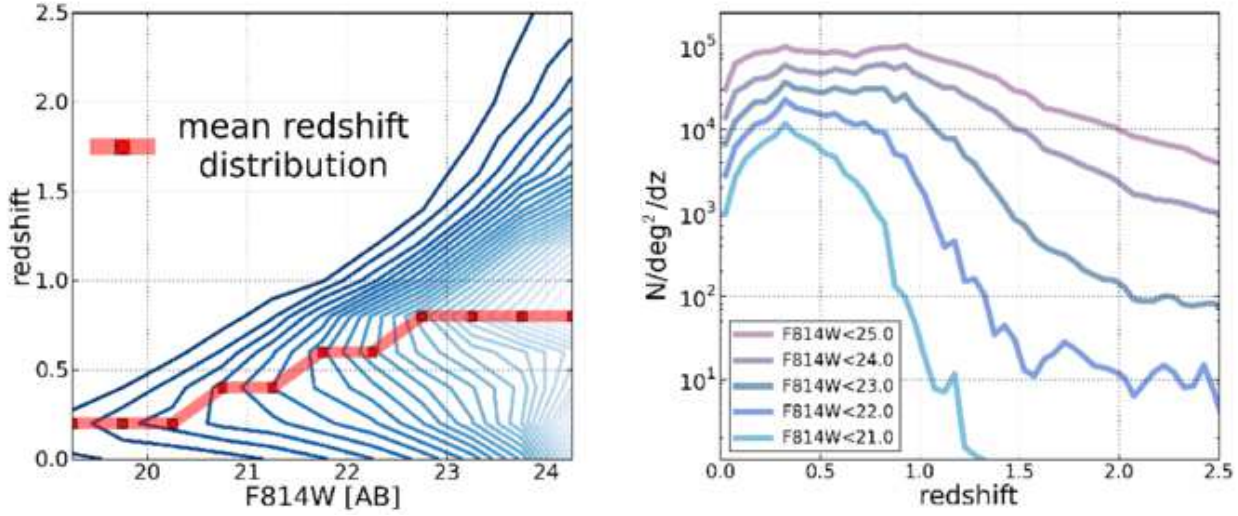


Figure 32. Evolution of the redshift distribution. The left panel shows the evolution of the averaged redshift distribution for the ALHAMBRA fields, as a function of the magnitude F814W. The mean redshift distribution (solid red line) indicates a clear evolution moving from a $\langle z \rangle \sim 0.2$ for F814W < 20.5 to a $\langle z \rangle \sim 0.86$ for F814W > 23.0. The right panel shows the averaged distribution of galaxies for the ALHAMBRA fields, as a function of the redshift for different ranges in magnitude.

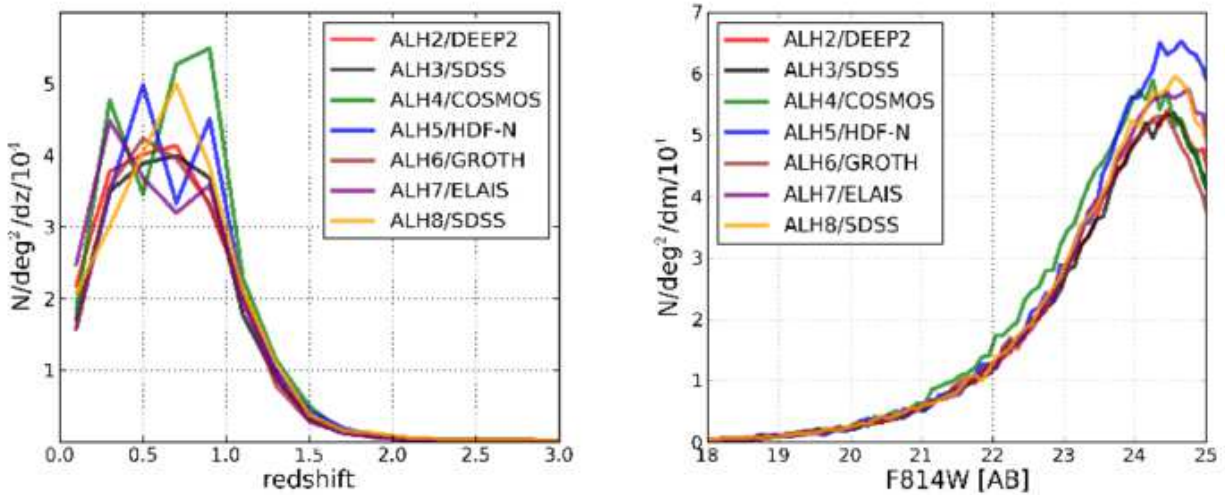


Figure 33. Effect of the cosmic variance in the $P(z)$. The left panel shows the redshift probability distribution function $P(z)$ for all the seven ALHAMBRA fields, using a range in magnitudes between $19.0 < F814W < 23.5$. The different ALHAMBRA fields are color-coded as indicated in the legend. Once again the ALHAMBRA-04 field associated with the COSMOS fields (green line) shows a peculiar distribution with a prominent peak at redshift $z \sim 0.86$. The right panel shows the cumulative number counts for the seven fields. Again the ALHAMBRA-4 field (green line) shows a clear excess in the number of galaxies detected per magnitude range with respect to the other fields.

parameter to $DZ = 2 * 0.0125 * (1+z)$ since this quantity corresponds to twice the expected sigma. The completeness factor (fraction of galaxies per *Odds* interval) as a function of F814W magnitude is presented in Fig. 36.

4.6 Emission-line galaxies

When representing the *Odds* distribution as a function of F814W magnitude for all galaxies, we see a clear locus at magnitudes in between $18 < F814W < 23$ and $0.0 < Odds < 0.1$. When representing

the logarithmic χ^2 distribution over the former *Odds* vs magnitude diagram, it immediately reveals those detections to have the highest χ^2 values and so the worst SED-fitting results to the galaxy templates, as illustrated in Fig. 37.

Detections with unexpected poor χ^2 fitting (given its magnitude) could be due to unreported photometric flaws worsening its SED-fitting performance or to an incomplete library of templates used to fit the data with. After purging the sample for every photometrically flagged detection, remaining galaxies within that locus were classified in two different groups: 1. unresolved stellar pairs

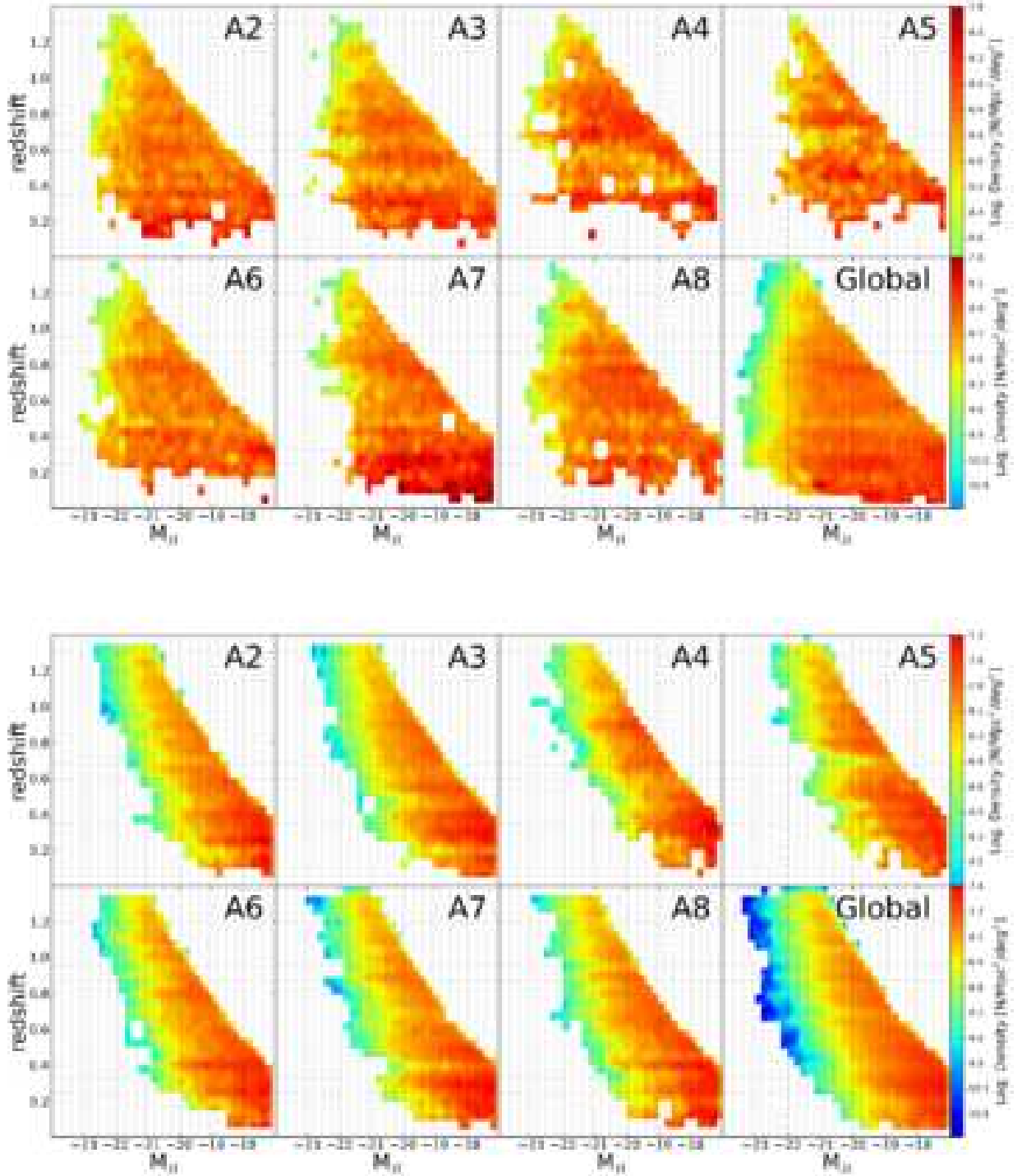


Figure 34. Redshift distribution in the rest-frame per ALHAMBRA field. We explored the variance in the redshift-magnitude distribution of galaxies as a function of the absolute B magnitude and the spectral-type. After splitting the sample among early-type galaxies (top panel, defined as $1 < T_b < 5$) and late-type galaxies (bottom panel, defined as $7 < T_b < 11$), we compared the resulting distributions among each of the 7 individual ALHAMBRA fields (A_i) + 1 averaged sample (*Global*). As observed from the panels, where the logarithmic density is color-coded, whereas each individual field shows clear and identifiable structures at different redshifts, the global samples show a more smooth distribution. In particular, we find that the well-known bimodal distribution in the COSMOS field (A4) is not systematically observed along the other fields, emphasizing the effects of cosmic variance on galaxy evolution studies.

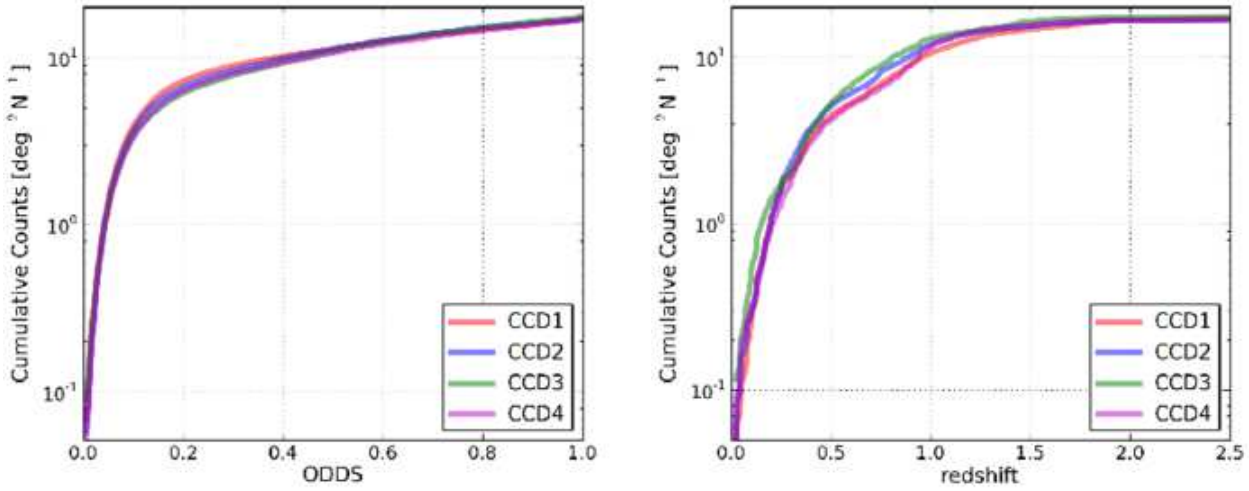


Figure 35. Internal photometric redshift checks. Following the same approach as explained in Section 3.8, we systematically compared the *Odds* (left panel) and photometric redshift z_b (right panel) distributions among contiguous CCDs. The statistical results were consistent between each other with a scatter within the expected intrinsic variance for the sample imaged by each detector. These test served to assure the homogeneity within the different fields.

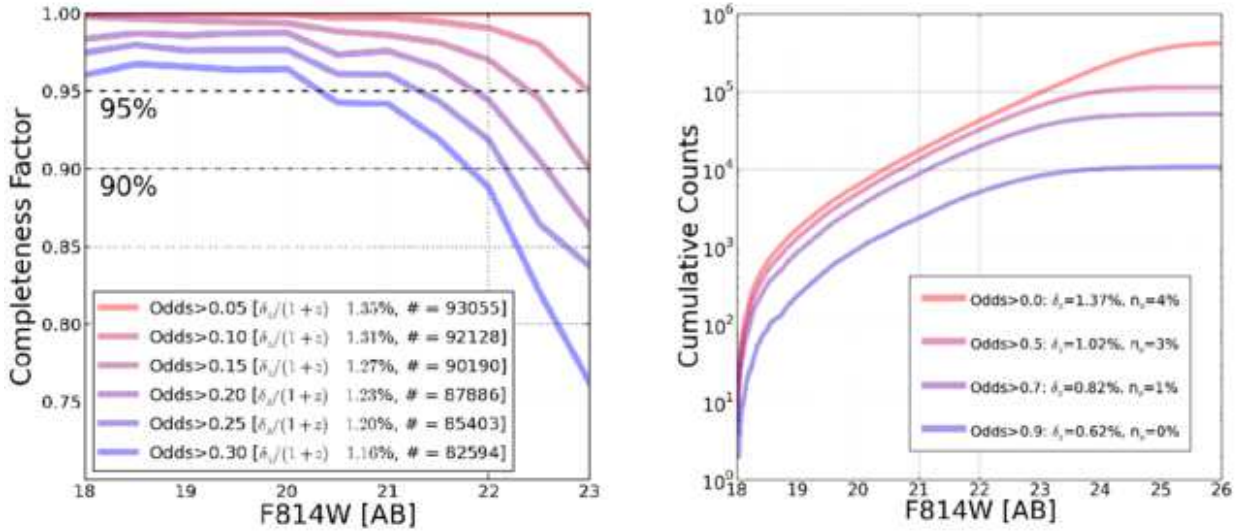


Figure 36. Photometric Redshift Depth. In order to characterize the photometric redshift depth for the ALHAMBRA catalogues, we quantified the amount of galaxies per *Odds* interval, which is equivalent to estimate the fraction and distribution of galaxies with a certain photometric redshift accuracy. As seen in the left panel, we explored the expected Completeness Factor as a function of the magnitude F814W and *Odds* interval. The total fraction of galaxies within each interval is specified in the legend. Similarly, the right panel shows the Cumulative distribution of galaxies as a function of the F814W magnitude for different *Odds* intervals. The expected accuracy for the photometric redshifts δ_z and the fraction of catastrophic outliers n_o (according to the spectroscopic sample) is indicated in the legend.

(identified as a single detection by SExtractor) with clearly asymmetric morphologies (spite of its photometric colors) and 2. very strong broad emission-line objects. As mentioned in Section 4, neither AGN nor QSO templates were included in the BPZ library and therefore these sources might be expected to be flagged by its poor-ness when accommodated to any BPZ template. As illustrated in left panel of Fig. 37, a fraction of $\sim 0.1\%$ active galaxies was found along the ALHAMBRA fields with this technique. Given the high value of χ^2 , the resulting photometric redshifts are (in most cases)

assigned by the prior probability and so favoring solutions at redshift $z_b \sim 0.4$ with intermediate spectral-types *Tb* (E0/Scd/Sbc).

5 PHOTOMETRIC CATALOGS

As explained in Section 3.5, we have generated homogeneous F814W-based catalogs across the 3.0 deg² combining the available information from our 23 + 1 photometric filters. The full area is

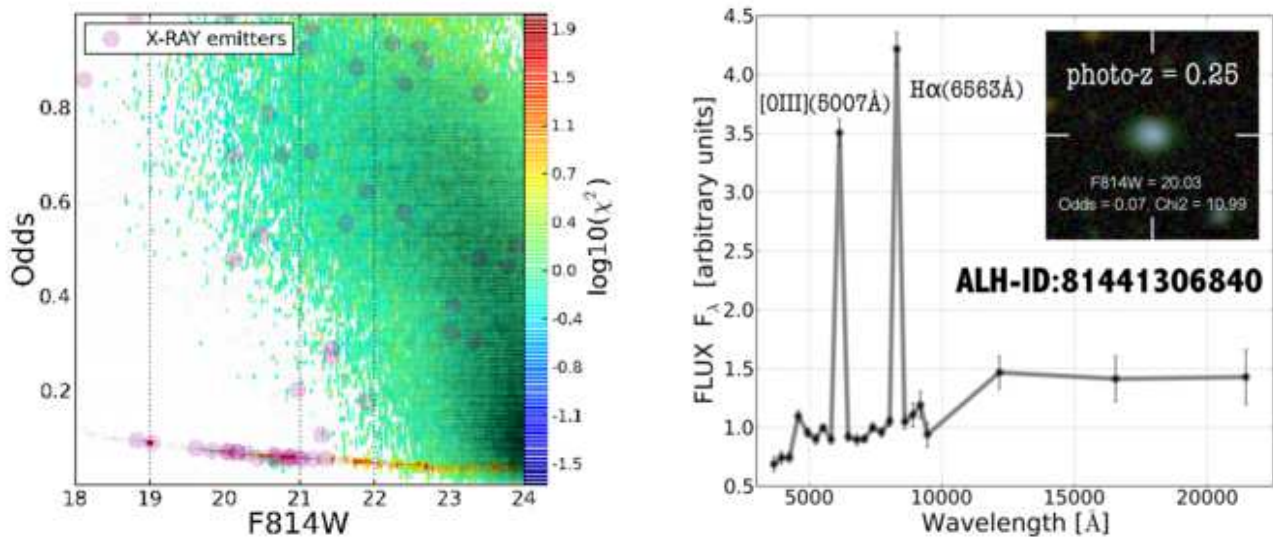


Figure 37. Emission-line galaxies identification. The left panel shows the *Odds* distribution as a function of magnitude F814W for the complete catalogue (stars excluded). As expected, there is a clear dependency between the *Odds* and the magnitude, indicating how the photometric redshifts confidence decreases with the S/N. We observed an unexpected locus for magnitudes in between $18 < \text{F814W} < 24$ and *Odds* in between $0.0 < \text{Odds} < 0.1$. When representing the logarithmic χ^2 distribution, it revealed those detections to have extremely high χ^2 values when SED-fitting the BPZ galaxy templates. We observed that those sources were mostly composed by very strong broad emission-line objects, AGNs and QSOs, galaxy types not included in the BPZ library of templates. The right panel shows an example of an intense emission-line galaxy within that horizontal sequence.

then divided in 48 individual catalogues containing the information listed in Appendix C1 & C2.

Unique IDs are given to every detection according to the following criteria: ID = 81442100119 stands for 814 (detection image) + 4 (field) + 2 (pointing) + 1 (CCD) + 00119 (Color-Pro_ID). Both astrometric and geometrical information is therefore derived from its corresponding F814W detection image: f04p02_F814W_1.swp.fits (following former example). SExtractor detection parameters were settled differently for every detection image as discussed in Section 3.5.2. Kron apertures (RK) and fraction-of-light radii (RF) were settled according to the aperture parameters defined in Table D1. Total magnitudes and empirically corrected uncertainties (Section 3.7) are given by all the 24 filters. Along with this, F814W_3arc represent F814W magnitudes measured on a 3" circular apertures and ditto F814W_3arc_corr but corrected to tied COSMOS/F814W photometry (Section 3.5). As every detection in the ALHAMBRA fields was covered by all the 24 filters, *nfd* indicates the number of filters a source was detected. Whenever a source was not detected, its magnitude was set to 99. and its photometric uncertainty replaced by a $1-\sigma$ upper limit (Section 6.1) suitable for BPZ.

Final catalogues contain several quality flag. *PhotoFlag* corresponds to the standard SExtractor photometric flag (Bertin & Arnouts 1996), *Satur_Flag* indicates a possible saturated source (typically stars with magnitudes brighter than F814W=16), *Stellar_Flag* represents a source-by-source statistical classification among stars and galaxies (Section 3.6), *irms_OPT_Flag* and *irms_NIR_Flag* indicates the number of optical and NIR bands a detection was observed with a normalized exposure time below its 80%, respectively. The *DupliDet_Flag* indicates either a source was detected twice (within the overlapping area among consecutive detectors). If so, the detection with the poorest S/N is set to a

value *DupliDet_Flag* = 1. Therefore, selecting detections with *DupliDet_Flag* = 0 removes all duplicated detections when combining catalogues.

The most likely photometric redshift solution for every source is assigned by *zb*. Additionally, *zb_min* and *zb_max* represent the lower and upper limits for the first peak within a 95% interval. Spectral-type classification is given by *tb_1* where its number refers to the selected template as indicated in Fig. 21. *Odds* gives the amount of redshift probability enclosed around the main peak (see Section 4) and χ^2 the reduced chi-squared from the comparison between observed and predicted fluxes according to the selected template and redshift. An estimation of each detection stellar mass content (in units of $\log_{10}(M_{\odot})$) is given by *Stell_Mass*. *M_ABS* corresponds to the absolute (AB) magnitude for the Johnson B-band. *MagPrior* corresponds to the F814W magnitude used to derived the BPZ Prior. Finally *z_ml* and *t_ml* represent again the photometric redshift and its spectral-type but estimated using a maximum likelihood without priors (instead of a Bayesian approach).

6 THE ALHAMBRA GOLD CATALOGUE

The ALHAMBRA gold catalogue corresponds to a subsample of $\sim 100\text{k}$ bright galaxies ($17 < \text{F814W} < 23$) with very accurate and reliable photometric redshifts with an expected error $\sigma_z < 0.012$ and redshift probability distribution functions $P(z)$ well-defined by a single Gaussian peak. The catalogue also includes PSF-corrected photometry for $\sim 20,000$ stars in the galactic halo (identified according to the methodology described in Section 3.6) along with ~ 1000 AGN candidates according to the analysis discussed in Section 4.6.

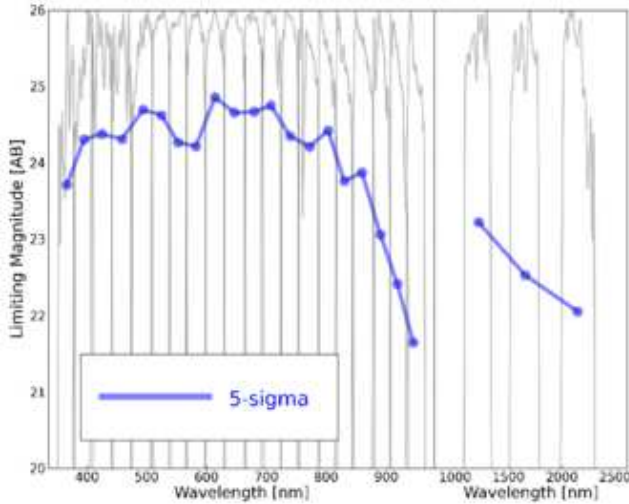


Figure 38. Limiting magnitudes. We derived limiting magnitudes for every image, as they represent a very useful piece of information during the SED-fitting procedure. As required by BPZ, we replaced galaxies with measured fluxes equal or lower than the estimation of the background signal by an upper limit defined as $1-\sigma$ above the background. Since limiting magnitudes depends on the photometric uncertainties, we computed limiting magnitudes after reestimating empirically the photometric errors. Meanwhile, we calculated the expected limiting magnitude using fixed apertures of $3''$ and $5-\sigma$, as seen in the figure. These magnitudes correspond to the averaged values for the complete set of images.

The ALHAMBRA gold catalog can be downloaded from the website: <http://cosmo.iaa.es/content/alhambra-gold-catalog>

6.1 Limiting Magnitudes

For sources only detected on its F814W detection image, an upper limit (defined as $1-\sigma$ above the background) is provided. These limiting magnitudes represent the deepest magnitudes extractable from an image providing an useful information during SED-fitting analysis. Limiting magnitudes are applied whenever measured fluxes, inside a fixed aperture, are equal or lower than the estimation of the background signal. Since limiting magnitudes depends directly on photometric errors, we computed limiting magnitudes after reestimating photometric errors, via empirical sigma estimation (Section 3.7). Derived limiting magnitudes for each band can be found within the photometric catalogues. In Fig. 38 we represent the averaged $5-\sigma$ limiting magnitudes for all the 23 bands using fixed circular apertures of $3''$.

7 SUMMARY

The ALHAMBRA (Advance Large Homogeneous Area Medium Band Redshift Astronomical) survey has observed 8 different regions of the sky, including sections of the COSMOS, DEEP2, ELAIS, GOODS-N, SDSS and Groth fields using a new photometric system with 20 contiguous $\sim 300\text{\AA}$ filters covering the optical range, combining them with deep *JHKs* imaging. The observations, carried out with the Calar Alto 3.5m telescope using the

wide field (0.25 deg^2 FOV) optical camera LAICA and the NIR instrument Omega-2000, correspond to ~ 700 hrs of on-target science images. The photometric system was specifically designed to maximize the effective depth of the survey in terms of accurate spectral-type and photometric redshift estimation along with the capability of identification of relatively faint emission lines.

Synthetic HST/ACS F814W detection images were generated to be able to define a constant and homogeneous window for all the ALHAMBRA fields. These images, photometrically complete down to a magnitude $F814W \leq 25.5$ AB, served not only to improve the quality of the photometric detections but also to carry out systematic comparisons with the COSMOS-survey. In order to improve the source detection efficiency, we masked every saturated star, stellar spike, ghost and damaged area. To minimize the variation of the image RMS, all flagged pixels were replaced with background noise.

To deal with the observed PSF-variability across filters, *ColorPro* (Coe et al. 2005) was used to perform accurate aperture-matched PSF-corrected photometry retrieving robust photometric colors ideal for photometric redshift estimations. For this purpose PSF-models were generated for individual images by manually selecting hundredth of non saturated and well isolated stars across the field. Using a compilation of $\sim 20,000$ stars, the mean radial PSF variation was smaller than 5%, enabling the usage of a single PSF-model per image.

We designed a set of simulations to test the accuracy of *ColorPro* retrieving precise photometry, across images with varied PSF. We degraded ACS/HST images (from COSMOS) to the typical condition of ALHAMBRA (in terms of PSF and background noise) and run *ColorPro* on it expecting retrieve null colors (equal magnitudes) for a sample of galaxies when observed under different PSFs. We found that the simulated colors showed a dispersion of $\sigma \sim 0.03$ for sources brighter than magnitude $F814W = 23.0$ and a $\sigma < 0.05$ for sources with magnitudes in between $23 < F814W < 24$, with negligible biases. We also used the simulations to study the expected photometric completeness for the ALHAMBRA fields. So, we derived the statistical probability of detecting a sample of faint galaxies when observed through the typical ALHAMBRA observational conditions. The result indicates that ALHAMBRA is photometrically complete down to a magnitude of $F814W \sim 24$. For fainter magnitudes, the number of detections decreases rapidly with a percentage of missed galaxies with magnitude $F814W > 25$ of $\sim 40\%$.

To decontaminate extragalactic sources from field stars, we developed a statistical classification method where every detection was classified in terms of the probability of being a star or a galaxy, given its apparent geometry, F814W magnitude, optical F489W-F814W and NIR J-Ks colors. We tested the goodness of our statistical classification by comparing the density of finding stars against that predicted by the Trilegal software (Girardi 2002, 2005). We found a very good agreement between both samples. When this statistical criteria is applied to the complete catalogue, we observed that stars dominate the sample down to a magnitude $F814W < 19$. For fainter magnitudes, the fraction of stars among galaxies rapidly declines with a contribution of $\sim 1\%$ for magnitudes $F814W = 22.5$. We retrieve an averaged stellar density in the galactic halo of ~ 7000 stars per deg^2 (~ 450 stars per CCD) for sources brighter than $F814W = 22.5$.

Given the correlation among pixels introduced during image processing, we empirically re-calculated photometric uncertain-

ties for every detection following a similar approach as that described in Labbé et al. (2003), Gawiser et al. (2006) and Quadri et al. (2007). Spanning a range of radius between 1-250 pixels, we thrown $\sim 50,000$ apertures on blank areas across the images to measure both the enclosed background signal and its scatter. The methodology served to properly estimate the empirical dependence between any galaxy photometric aperture and its photometric uncertainty.

We calculated photometric redshifts with the BPZ2.0 code (Benítez 2013, in prep). This new version includes a new prior empirically derived for each spectral-type and magnitude by fitting luminosity functions provided by GOODS- MUSIC (Santini et al. 2009), COSMOS (Scoville et al. 2007) and UDF (Coe et al. 2006), a new empirically calibrated library of galaxy templates and an estimation of the galaxy stellar mass based on the color-M/L ratio relationship established by Kannappan (2007a).

Given the overlap between the ALHAMBRA fields and other existing spectroscopic surveys, we compiled a sample of ~ 7200 galaxies with secure spectroscopic redshifts, mostly covering the ALHAMBRA parameter space, i.e., with a redshift range $0 < z_s < 1.5$ ($\langle z_s \rangle \sim 0.77$) and a magnitude range (based on ALHAMBRA photometry) $18 < F814W < 25$ ($\langle F814W \rangle \sim 22.3$). Based on this spectroscopic sample, our photometric redshifts have a precision of $\delta_z/(1+z_s) = 1\%$ for $I < 22.5$ and $\delta_z/(1+z_s) = 1.4\%$ for $22.5 < I < 24.5$. Precisions of $\delta_z/(1+z_s) < 0.5\%$ are reached for the brighter spectroscopic sample, showing the potential of medium-band photometric surveys.

We refined photometric zeropoints derived using standard stellar-based calibration techniques, by comparing the observed colors of galaxies (for which spectroscopic redshifts were available) with those expected by the BPZ library of templates. We found that the so-derived corrections improved not only improved the photometric redshifts accuracy but also reduced the fraction of catastrophic outliers. Considering the possibility of a systematic effect during the data reduction, we represented globally the zero-point corrections for the all the individual images as a function of the AIRMASS, the Stellar Symmetry, the FWHM Scatter, differences between PSFs-models and stars, magnitude ranges, redshift ranges or aperture sizes. No clear correlations were observed with typical fluctuations smaller than 3%. We therefore conclude that the zeropoint offsets do not depend on the photometric treatment and represent real differences between the calibration obtained from traditional color transformations based on stars and the average colors of galaxies as defined by the BPZ template set, calibrated with HST observations.

For those fields without spectroscopic coverage, a new methodology (described in this work) was applied to calibrate photometric zeropoint estimations using photometric redshifts. Essentially, we realized that the photometric redshifts obtained for emission line galaxies were quite robust to changes in the zeropoint calibration and therefore could be treated as spectroscopic for calibration purposes, obtaining an automatic and self-contained zeropoint correction for all our fields. This methodology not only successfully improved the photometric redshifts accuracy (almost up to the level provided by the spectroscopic sample), but also dramatically reduced the fraction of catastrophic outliers, avoiding serious problem of inhomogeneity among fields.

Considering the probabilistic nature of the photometric redshift estimations, we made use of the complete information yielded

by the probability distribution functions $P(z, T|C)$ (Benítez 2000, Coe et al. 2006, Mandelbaum et al. 2008; Cunha et al. 2009; Wittman 2009; Bordoloi et al. 2010; Abrahamse et al. 2011; Sheldon et al. 2012). This approach represents a more convenient estimator for most faint galaxies as the $p(z)$ usually becomes multimodal and completely asymmetric, so not well represented by a single and symmetric (Gaussian-like) distribution. Using the complete probability distribution functions we found that the global photometric redshift distribution shows a mean redshift $\langle z \rangle = 0.56$ for $I < 22.5$ AB and $\langle z \rangle = 0.86$ for $I < 24.5$ AB. In particular, comparison with our average $n(z)$ shows that the COSMOS field has a rather peculiar redshift distribution, with a large spike a $z \sim 0.7$ and an underdensity for $z < 0.5$ which mimics a significant redshift density evolution effect.

We explored the cosmic variance effect in the redshift distribution of galaxies as a function of the absolute B magnitude and the spectral-type. We found that the well-known bimodal distribution in the COSMOS field was not systematically observed along the other fields, emphasizing the usefulness of the ALHAMBRA data on galaxy evolution studies.

We discovered a new methodology to identify potential AGN candidates using BPZ. When representing the Odds distribution as a function of F814W magnitude for all galaxies, we saw an unexpected locus at magnitudes in between $18 < F814W < 23$ and $0.0 < Odds < 0.1$. When representing the logarithmic χ^2 distribution over the former Odds vs magnitude diagram, it revealed those detections to have the highest χ^2 values and so the worst SED-fitting results to the galaxy templates (Fig. 37). After purging the sample for photometrically flagged detections, remaining galaxies within that locus were classified in two different groups: 1. unresolved stellar pairs with clearly asymmetric morphologies (spite of its photometric colors) and 2. very strong broad emission-line objects, AGNs or variable sources. All galaxy types not included in the BPZ library of templates.

The PSF-corrected multicolor photometry and photometric redshifts for $\sim 438,000$ galaxies presented in this work, covers an effective area of 2.79 deg^2 , split into 14 strips of $58.5' \times 15.5'$ and represents a ~ 32 hrs of on-target exposure time. Given its depth, multiband coverage and a much smaller cosmic variance than other similar projects, ALHAMBRA is a unique dataset for galaxy evolution studies. Several of the techniques presented here will have a wide applicability to future large scale narrow band photometric redshift surveys like JPAS (Javalambre Physics of the Accelerated Universe, Benítez 2009a, Benítez 2013, in prep.).

ACKNOWLEDGMENTS

We acknowledge support from the Spanish Ministerio de Educación y Ciencia through grant AYA2006-14056 BES-2007-16280. We acknowledges the financial support from the Spanish MICINN under the Consolider-Ingenio 2010 Program grant CSD2006-00070: First Science with the GTC. Part of this work was supported by Junta de Andalucía, through grant TIC-114 and the Excellence Project P08-TIC-3531, and by the Spanish Ministry for Science and Innovation through grants AYA2006-1456 and AYA2010-15169.

REFERENCES

Abrahamse, A., Knox, L., Schmidt, S., et al. 2011, *ApJ*, 734, 36

Aparicio Villegas, T., Alfaro, E. J., Cabrera-Caño, J., et al. 2010, *AJ*, 139, 1242

Barger, A. J.; Cowie, L. L.; Wang, W.-H. 2008, *ApJ*, 689, 687

Baum, W. A. 1962, *IAU Symp. 15: Problems of Extra-Galactic Research*, 15, 390

Benítez, N. 2000, *ApJ*, 536, 571

Benítez N., Ford, H., Bouwens, R., et al. 2004, *ApJ*, 150, 1

Benítez, N., Gaztañaga, E., Miquel, R., et al. 2009, *ApJ*, 691, 241

Benítez N., et al., 2009, *ApJ*, 692L 5B

Bernardi, M., Shankar, F., Hyde, J. B., et al. 2010, *MNRAS*, 404, 2087

Bertin, E. & Arnouts, S. 1996, *A&A*, 117, 393

Bertin, E., Mellier, Y., Radovich, M., et al. 2002, *Astronomical Data Analysis Software and Systems XI*, 281, 228

Bohlin, R. C. 2007, *The Future of Photometric, Spectrophotometric and Polarimetric Standardization*, 364, 315

Bongiovanni, A., Oteo, I., Cepa, J., et al. 2010, *A&A*, 519, L4

Bordoloi, R., Lilly, S. J., & Amara, A. 2010, *MNRAS*, 406, 881

Brammer, G. B., van Dokkum, P. G., & Coppi, P. 2008, *ApJ*, 686, 1503

Bundy, K., Ellis, R. S., Conselice, C. J., et al. 2006, *ApJ*, 651, 120

Capak et al., 2007, *ApJS*, 172, 99

Cardamone et al., 2010, *ApJS*, 189, 270

Casertano, S., de Mello, D., Dickinson, M., et al. 2000, *AJ*, 120, 2747

Coe, D., Benítez, N., Sánchez, S. F., et al. 2006, *AJ*, 132, 926. & Brunner, R. J. 1997, *ApJ*, 486, L11

Cristóbal-Hornillos, D., Aguerri, J. A. L., Moles, M., et al. 2009, *ApJ*, 696, 1554

Csabai, I., Budavári, T., Connolly, A. J., et al. 2003, *AJ*, 125, 580

Cunha, C. E., Lima, M., Oyaizu, H., Frieman, J., & Lin, H. 2009, *MNRAS*, 396, 2379

Cutri, R. M., Skrutskie, M. F., van Dyk, S., et al. 2003, "The IRSA 2MASS All-Sky Point Source Catalog, NASA/IPAC Infrared Science Archive.

Daddi, E., Cimatti, A., Renzini, A., et al. 2004, *ApJ*, 617, 746

Dahlen, T., Mobasher, B., Dickinson, M., et al. 2010, *ApJ*, 724, 425

de Santis, C., Grazian, A., Fontana, A., & Santini, P., *New Astron.* 2007, 12, 271

Fernández-Soto, A., Lanzetta, K. M., & Yahil, A. 1999, *ApJ*, 513, 34

Fernández-Soto, A., Lanzetta, K. M., Chen, H.-W., Pascarelle, S. M., & Yahata, N. 2001, *ApJs*, 135, 41

Fioc, M., & Rocca-Volmerange, B. 1997, *A&A*, 326, 950

Gawiser, E., van Dokkum, P. G., Herrera, D., et al. 2006, *ApJs*, 162, 1

Girardi, L., Bertelli, G., Bressan, A., et al. 2002, *A&A*, 391, 195

Girardi, L., Groenewegen, M. A. T., Hatziminaoglou, E., & da Costa, L. 2005, *A&A*, 436, 895

Gregg, M. D., et al. 2004, *Bulletin of the American Astronomical Society*, 36, 1496

Labbé, I., Franx, M., Rudnick, G., et al. 2003, *AJ*, 125, 1107

Laidler, V. G., Grogan, N., Clubb, K., et al. 2006, *Astronomical Data Analysis Software and Systems XV*, 351, 228

Hickson, P., Gibson, B. K., & Callaghan, K. A. S. 1994, *MNRAS*, 267, 911

Hickson, P. & Mulrooney, M. K. 1998, *Astrophys. J. (Suppl.)*, 115, 35-42

Hildebrandt, H., Wolf, C., & Benítez, N. 2008, *A&A*, 480, 703

Ilbert, O., Arnouts, S., McCracken, H. J., et al. 2006, *A&A*, 457, 841

Ilbert, O., Capak, P., Salvato, M., et al. 2009, *ApJ*, 690, 1236

Johnson, H. L., & Morgan, W. W. 1953, *ApJ*, 117, 313

Kannappan, S. J., & Gawiser, E. 2007, *ApJL*, 657, L5

Lanzetta, K. M., Yahil, A. & Fernández-Soto, A. 1996, *Nature*, 381, 759

Madau, P. 1995, *QSO Absorption Lines*, 377

Mandelbaum, R., Seljak, U., Hirata, C. M., et al. 2008, *MNRAS*, 386, 781

Massey, P., & Gronwall, C. 1990, *ApJ*, 358, 344

Matute, I., Márquez, I., Masegosa, J., et al. 2012, *A&A*, 542, A20

Merson, A. I., Baugh, C. M., Helly, J. C., et al. 2013, *MNRAS*, 429, 556

Mitchell, P. D., Lacey, C. G., Baugh, C. M., & Cole, S. 2013, *arXiv:1303.7228*

Moles, M., et al. 2008, *AJ*, 136, 1325

Oke, J. B. 1990, *AJ*, 99, 1621

Oke, J. B., & Gunn, J. E. 1983, *AJ*, 266, 713

Pérez-González, P. G., Cava, A., Barro, G., et al. 2013, *ApJ*, 762, 46

Postman, M., Coe, D., Benítez, N., et al. 2012, *ApJS*, 199, 25

Quadri, R., Marchesini, D., van Dokkum, P., et al. 2007, *AJ*, 134, 1103

Rowan-Robinson, M., Babbedge, T., Oliver, S., et al. 2008, *MNRAS*, 386, 697

Santini, P., Fontana, A., Grazian, A., et al. 2009, *VizieR Online Data Catalog*, 350, 40751

Sawicki, M. J., Lin, H., & Yee, H. K. C. 1997, *AJ*, 113, 1

Schlegel, D. J., Finkbeiner, D. P., Davis, M., 1998, *ApJ*, 500 525

Scoville, N., Abraham, R. G., Aussel, H., et al. 2007, *ApJS*, 172, 38

Sheldon, E. S., Cunha, C. E., Mandelbaum, R., Brinkmann, J., & Weaver, B. A. 2012, *ApJS*, 201, 32

Stabenau H. F., Connolly A., Jain B., 2008, *MNRAS*, 387, 1215

Stetson, P. B. 1987, *PASP*, 99, 191

Stone, R. P. S. 1996, *ApJS*, 107, 423

Taniguchi, Y. 2004, *Studies of Galaxies in the Young Universe with New Generation Telescope*, 107

Tucker, D. L., Smith, J. A., & Brinkmann, J. 2001, *The New Era of Wide Field Astronomy*, 232, 13

Williams, R. E., Blacker, B., Dickinson, M., et al. 1996, *AJ*, 112, 1335

Wittman, D. 2009, *ApJ*, 700, L174

Wolf, C., Meisenheimer, K., Roser, H.-J. 2001, *A&A*, 365, 660

Wolf, C. et al. 2001a, *A&A*, 365, 681

Wolf, C., Meisenheimer, K., Kleinheinrich, M., et al. 2004, *A&A*, 421, 913

Wuyts et al. 2008, *ApJ*, 682, 985

APPENDIX A: THE ALHAMBRA FIELDS NOMENCLATURE.

In this appendix we illustrate an example of the Pointing layout for the ALHAMBRA fields. The combination of two contiguous pointing yields a final layout composed by two strips of $58.5' \times 15.5'$ (comprising four individual CCDs) with a separation of $\sim 13.0'$.

APPENDIX B: PHOTOMETRIC REDSHIFT SURVEYS COMPARISON

The figure represents the photometric redshift accuracy versus the covered area for several surveys (see Table 2). The number of photometric passbands is color-coded as described in the top-right panel. The marker-size represents logarithmically the number of detections.

APPENDIX C: PHOTOMETRIC REDSHIFT CATALOGUES DESCRIPTION.

In this appendix we include the description of the photometric redshift catalogues content in more detail.

APPENDIX D: SEXTRACTOR CONFIGURATION AND THE EFFECTIVE AREA.

In this appendix we present an example of the SExtractor configuration used to derive the F814W detections. Along with this, we also includes several tables containing statistical information concerning the observations.

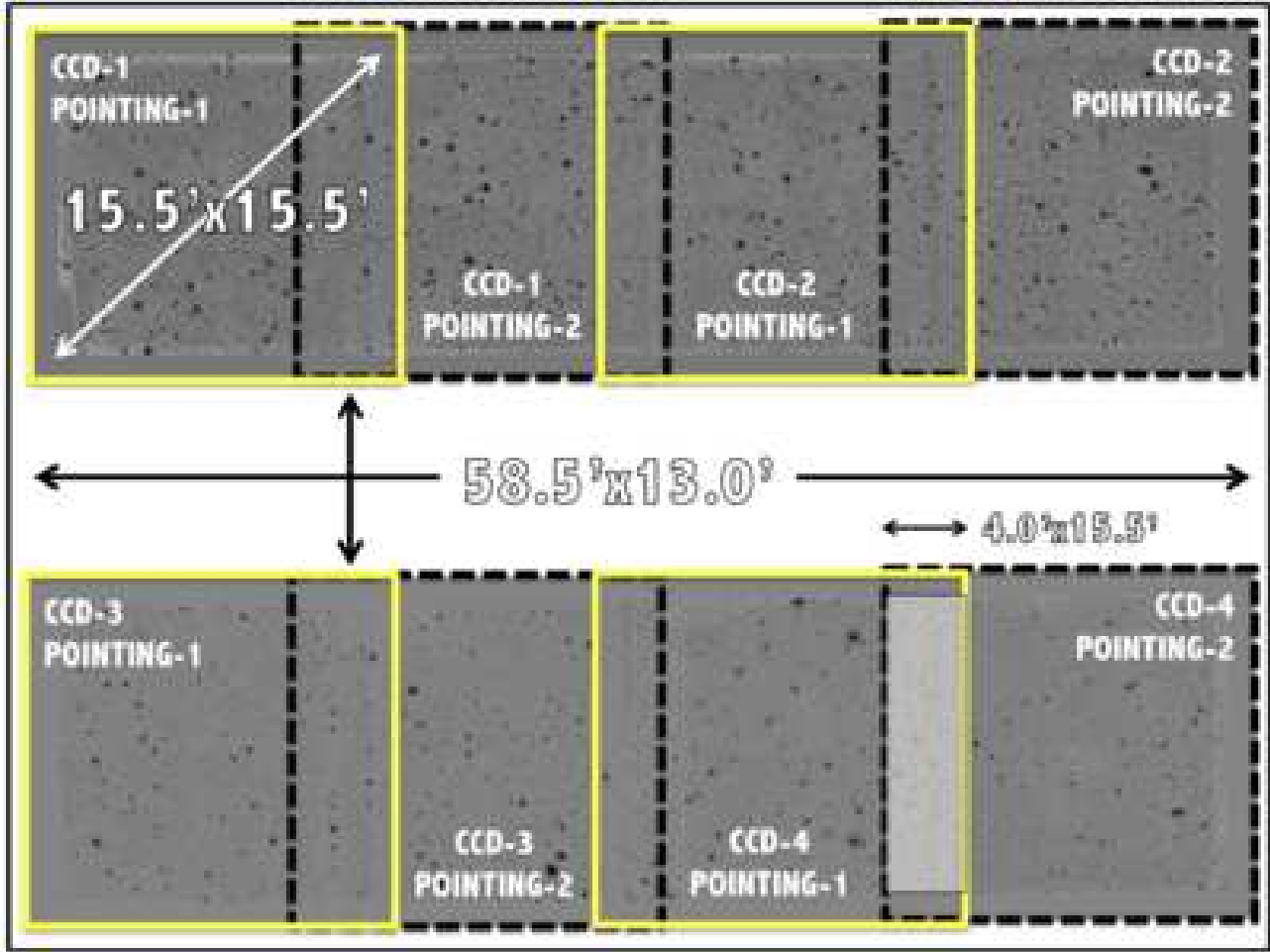


Figure A1. Pointing layout for the ALHAMBRA fields. Given the geometrical configuration of the optical imager LAICA, each pointing is composed by four CCDs (as marked with the yellow squares) with an internal gap of $\sim 13.0'$. The combination of two contiguous pointing yields a final layout composed by two strips of $58.5' \times 15.5'$ (comprising four individual CCDs) with a separation of $\sim 13.0'$. Contiguous CCDs within each strip show a maximum overlap of $4.0' \times 15.5'$.

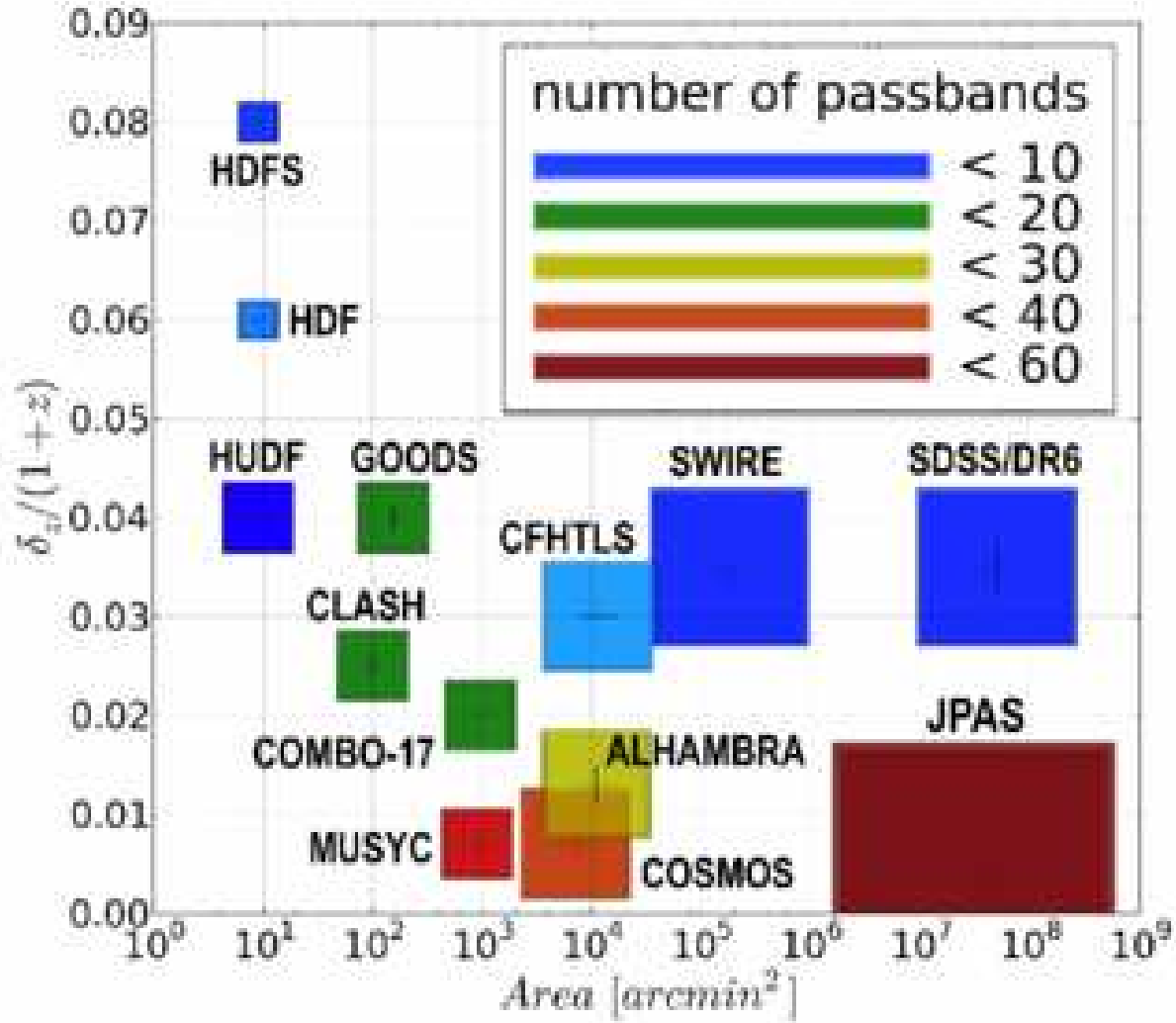


Figure B1. Photometric redshift surveys comparison. The figure represents the photometric redshift accuracy versus the covered area for several surveys (see Table 2). The number of photometric passbands is color-coded as described in the top-right panel. While the marker-size represents logarithmically the number of detections, the position of the internal plus sign indicates to its photometric redshift accuracy.

Table C1. The ALHAMBRA Photometric Redshift Catalogs Content. Part I

COLUMN	PARAMETER	DESCRIPTION
1	ID_ColorPro	Object ID Number
2	Field	ALHAMBRA field
3	Pointing	Pointing within the field
4	CCD	Detector within the pointing
5	RA	Right Ascension in decimal degrees [J2000]
6	DEC	Declination in decimal degrees [J2000]
7	XX	x pixel coordinate
8	YY	y pixel coordinate
9	AREA	Isophotal aperture area (pixels)
10	FWHM	Full width at half maximum (arcsec)
11	STELL	SExtractor 'stellarity' (1 = star; 0 = galaxy)
12	ELL	Ellipticity = 1 - B/A
13	a	Profile RMS along major axis (pixels)
14	b	Profile RMS along minor axis (pixels)
15	THETA	Position Angle (CCW/x)
16	RK	Kron apertures in units of A or B (pixels)
17	RF	Fraction-of-light radii (pixels)
18	S/N	Signal to Noise (SExt_FLUX_AUTO/SExt_FLUXERR_AUTO)
19	PhotoFlag	SExtractor Photometric Flag
20,21	F365W, dF365W	F365W total magnitude & uncertainty
22,23	F396W, dF396W	F396W total magnitude & uncertainty
24,25	F427W, dF427W	F427W total magnitude & uncertainty
26,27	F458W, dF458W	F458W total magnitude & uncertainty
28,29	F489W, dF489W	F489W total magnitude & uncertainty
30,31	F520W, dF520W	F520W total magnitude & uncertainty
32,33	F551W, dF551W	F551W total magnitude & uncertainty
34,35	F582W, dF582W	F582W total magnitude & uncertainty
36,37	F613W, dF613W	F613W total magnitude & uncertainty
38,39	F644W, dF644W	F644W total magnitude & uncertainty
40,41	F675W, dF675W	F675W total magnitude & uncertainty
42,43	F706W, dF706W	F706W total magnitude & uncertainty
44,45	F737W, dF737W	F737W total magnitude & uncertainty
46,47	F768W, dF768W	F768W total magnitude & uncertainty
48,49	F799W, dF799W	F799W total magnitude & uncertainty
50,51	F830W, dF830W	F830W total magnitude & uncertainty
52,53	F861W, dF861W	F861W total magnitude & uncertainty
54,55	F892W, dF892W	F892W total magnitude & uncertainty
56,57	F923W, dF923W	F923W total magnitude & uncertainty
58,59	F954W, dF954W	F954W total magnitude & uncertainty
60,61	J, dJ	NIR-J total magnitude & uncertainty
62,63	H, dH	NIR-H total magnitude & uncertainty
64,65	KS, dKS	NIR-KS total magnitude & uncertainty
66,67	F814W, dF814W	F814W total magnitude & uncertainty
68	F814W_3arcs	3arcsec Circular Aperture magnitude [AB]
69	dF814W_3arcs	3arcsec Circular Aperture magnitude uncertainty [AB]
70	F814W_3arcs_corr	Corrected 3arcsec Circular Aperture Magnitude [AB]
71	nfd	Number Filters Detected (out of 24)
72	xray	X-Ray Source [0:NO,1:YES] (2XMM;Watson et al. 2009)
73	PercW	Percentual Photometric Weight (on detection image).
74	Satur_Flag	Photometric Saturation-Flag [0:Good Detection, 1:Saturated Detection]
75	Stellar_Flag	Statistical STAR/GALAXY Discriminator [0:Galaxy,0.5:Unknown,1:Star]
76	DupliDet_Flag	Duplicated Detection Flag [0:Non duplicated, 1:Duplicated]

Table C2. Photometric Redshift Catalogs Content. Part II

COLUMN	PARAMETER	DESCRIPTION
77	zb	BPZ most likely redshift
78	zb_min	Lower limit (95p confidence)
79	zb_max	Upper limit (95p confidence)
80	tb	BPZ most likely spectral type
81	Odds	$P(z)$ contained within $zb \pm 2 \times 0.01 \times (1+z)$
82	z_ml	Maximum Likelihood most likely redshift
83	t_ml	Maximum Likelihood most likely spectral type
84	Chi2	Poorness of BPZ fit: observed vs. model fluxes
85	Stell_Mass	Stellar Mass ($\log_{10}(M_{\odot})$)
86	M_ABS	Absolute Magnitude [AB] (B_JOHNSON)
87	MagPrior	Magnitude Used for the Prior (F814W)
88	irms_F365W	Percentual Weight on F365W 1/RMS image (within ISOphtal Area).
89	irms_F396W	Percentual Weight on F396W 1/RMS image (within ISOphtal Area).
90	irms_F427W	Percentual Weight on F427W 1/RMS image (within ISOphtal Area).
91	irms_F458W	Percentual Weight on F458W 1/RMS image (within ISOphtal Area).
92	irms_F489W	Percentual Weight on F489W 1/RMS image (within ISOphtal Area).
93	irms_F520W	Percentual Weight on F520W 1/RMS image (within ISOphtal Area).
94	irms_F551W	Percentual Weight on F551W 1/RMS image (within ISOphtal Area).
95	irms_F582W	Percentual Weight on F582W 1/RMS image (within ISOphtal Area).
96	irms_F613W	Percentual Weight on F613W 1/RMS image (within ISOphtal Area).
97	irms_F644W	Percentual Weight on F644W 1/RMS image (within ISOphtal Area).
98	irms_F675W	Percentual Weight on F675W 1/RMS image (within ISOphtal Area).
99	irms_F706W	Percentual Weight on F706W 1/RMS image (within ISOphtal Area).
100	irms_F737W	Percentual Weight on F737W 1/RMS image (within ISOphtal Area).
101	irms_F768W	Percentual Weight on F768W 1/RMS image (within ISOphtal Area).
102	irms_F799W	Percentual Weight on F799W 1/RMS image (within ISOphtal Area).
103	irms_F830W	Percentual Weight on F830W 1/RMS image (within ISOphtal Area).
104	irms_F861W	Percentual Weight on F861W 1/RMS image (within ISOphtal Area).
105	irms_F892W	Percentual Weight on F892W 1/RMS image (within ISOphtal Area).
106	irms_F923W	Percentual Weight on F923W 1/RMS image (within ISOphtal Area).
107	irms_F954W	Percentual Weight on F954W 1/RMS image (within ISOphtal Area).
108	irms_J	Percentual Weight on J 1/RMS image (within ISOphtal Area).
109	irms_H	Percentual Weight on H 1/RMS image (within ISOphtal Area).
110	irms_KS	Percentual Weight on KS 1/RMS image (within ISOphtal Area).
111	irms_F814W	Percentual Weight on F814W 1/RMS image (within ISOphtal Area).
112	irms_OPT_Flag	Optical-Quality-Flag. Number of Optical Filters with PercW < 0.8
113	irms_NIR_Flag	NIR-Quality-Flag. Number of NIR Filters with PercW < 0.8

Table D1. Example of the typical SExtractor configuration used to derive the ALHAMBRA photometric catalogs. Asterisked parameters may vary among CCDs.

PARAMETER	SETTING	COMMENT
ANALYSIS_THRESH	1.3*	Limit for isophotal analysis σ
BACK_SIZE	256	Background mesh in pixels
BACK_FILTERSIZE	5	Background filter
BACKPHOTO_THICK	102	Thickness of the background LOCAL annulus
BACKPHOTO_TYPE	LOCAL	Photometry background subtraction type
CATALOG_NAME	STDOUT	Output to pipe instead of file
CATALOG_TYPE	ASCII	Output type
CLEAN	Y	Clean spurious detections
CLEAN_PARAM	1	Cleaning efficiency
CHECKIMAGE_TYPE	SEGMENTATION	Output Image Type
DETECT_MINAREA	8*	Minimum number of pixels above threshold
DEBLEND_MINCONT	0.0002	Minimum contrast parameter for deblending
DEBLEND_NTHRESH	64	Number of deblending sub-thresholds
DETECT_THRESH	1.35*	Detection Threshold in σ
DETECT_TYPE	CCD	Detector type
FILTER	Y	Use filtering
FILTER_NAME	tophat_3.0_3x3.conv	Filter for detection image
GAIN	57.68*	Gain is 1 for absolute RMS map
MAG_GAMMA	4.0	Gamma of emulsion
MAG_ZEROPOINT	0.*	Magnitude zero-point
MEMORY_PIXSTACK	2600000	Number of pixels in stack
MEMORY_BUFSIZE	4600	Number of lines in buffer
MEMORY_OBJSTACK	15000	Size of the buffer containing objects
MASK_TYPE	CORRECT	Correct flux for blended objects
PARAMETERS_NAME	ColorPro.param	Fields to be included in output catalog
PHOT_APERTURES	14.0	MAG_APER aperture diameter(s) in pixels
PHOT_AUTOPARAMS	2.5,3.5	MAG_AUTO parameters: <Kron_fact>,<min_radius>
PIXEL_SCALE	0.221	Size of pixel in arcseconds
SATUR_LEVEL	50000	Level of saturation
SEEING_FWHM	0.86*	Stellar FWHM in arcseconds
STARNNW_NAME	default.nnw	Neural-Network_Weight table filename
WEIGHT_TYPE	MAP_WEIGHT	Set Weight image type

Table D2. Effective Surveyed Area. The definition of the effective area is provided in section 3.5.3.

Field Name	Eff. Area [deg ²]	Field Name	Eff. Area [deg ²]
ALHAMBRA_F02P01C01	0.0580	ALHAMBRA_F06P01C01	0.0593
ALHAMBRA_F02P01C02	0.0584	ALHAMBRA_F06P01C02	0.0583
ALHAMBRA_F02P01C03	0.0540	ALHAMBRA_F06P01C03	0.0585
ALHAMBRA_F02P01C04	0.0582	ALHAMBRA_F06P01C04	0.0582
ALHAMBRA_F02P02C01	0.0596	ALHAMBRA_F06P02C01	0.0587
ALHAMBRA_F02P02C02	0.0506	ALHAMBRA_F06P02C02	0.0587
ALHAMBRA_F02P02C03	0.0538	ALHAMBRA_F06P02C03	0.0572
ALHAMBRA_F02P02C04	0.0586	ALHAMBRA_F06P02C04	0.0589
ALHAMBRA_F03P01C01	0.0586	ALHAMBRA_F07P03C01	0.0587
ALHAMBRA_F03P01C02	0.0589	ALHAMBRA_F07P03C02	0.0590
ALHAMBRA_F03P01C03	0.0578	ALHAMBRA_F07P03C03	0.0576
ALHAMBRA_F03P01C04	0.0592	ALHAMBRA_F07P03C04	0.0587
ALHAMBRA_F03P02C01	0.0592	ALHAMBRA_F07P04C01	0.0589
ALHAMBRA_F03P02C02	0.0577	ALHAMBRA_F07P04C02	0.0566
ALHAMBRA_F03P02C03	0.0569	ALHAMBRA_F07P04C03	0.0580
ALHAMBRA_F03P02C04	0.0590	ALHAMBRA_F07P04C04	0.0590
ALHAMBRA_F04P01C01	0.0589	ALHAMBRA_F08P01C01	0.0588
ALHAMBRA_F04P01C02	0.0590	ALHAMBRA_F08P01C02	0.0590
ALHAMBRA_F04P01C03	0.0569	ALHAMBRA_F08P01C03	0.0577
ALHAMBRA_F04P01C04	0.0589	ALHAMBRA_F08P01C04	0.0587
ALHAMBRA_F05P01C01	0.0595	ALHAMBRA_F08P02C01	0.0585
ALHAMBRA_F05P01C02	0.0594	ALHAMBRA_F08P02C02	0.0583
ALHAMBRA_F05P01C03	0.0588	ALHAMBRA_F08P02C03	0.0558
ALHAMBRA_F05P01C04	0.0594	ALHAMBRA_F08P02C04	0.0576